CCFE-PR(15)107

Jan S. Wróbel, Duc Nguyen-Manh, Mikhail Yu. Lavrentiev,
Marek Muzyk and Sergei L. Dudarev

Phase stability of ternary fcc and bcc Fe-Cr-Ni alloys

Phase stability of ternary fcc and bcc Fe-Cr-Ni alloys

Jan S. Wróbel, Duc Nguyen-Manh, Mikhail Yu. Lavrentiev, Marek Muzyk and Sergei L. Dudarev

CCFE, Culham Science Centre, Abingdon, Oxon OX14 3DB, UK

Phase stability of ternary fcc and bcc Fe-Cr-Ni alloys

Jan S. Wróbel,* Duc Nguyen-Manh, Mikhail Yu. Lavrentiev, Marek Muzyk, and Sergei L. Dudarev
CCFE, Culham Science Centre, Abingdon, Oxon OX14 3DB, UK
(Dated: August 21, 2014)

The phase stability of fcc and bcc magnetic binary Fe-Cr, Fe-Ni, Cr-Ni alloys and ternary Fe-Cr-Ni alloys is investigated using a combination of density functional theory (DFT), Cluster Expansion (CE) and Magnetic Cluster Expansion (MCE). Energies, magnetic moments, and volumes of more than 500 alloy structures are evaluated using DFT, and the most stable magnetic configurations are compared with experimental data. Deviations from the Vegard law in fcc Fe-Cr-Ni alloys, associated with non-linear variation of atomic magnetic moments as functions of alloy composition, are observed. Accuracy of the CE model is assessed against the DFT data, where for ternary alloys the cross-validation error is smaller than 12 meV/atom. A set of cluster interaction parameters is defined for each alloy, where it is used for predicting new ordered alloy structures. Fcc Fe_2CrNi phase with Cu_2NiZn-like structure is predicted as the global ground state with the lowest chemical ordering temperature of 650K. DFT-based Monte Carlo (MC) simulations are used for assessing finite temperature fcc-bcc phase stability and order-disorder transitions in Fe-Cr-Ni alloys. Enthalpies of formation of ternary alloys calculated from MC simulations at 1600K combined with magnetic correction derived from MCE are in excellent agreement with experimental values measured at 1565K. Chemical order is analysed, as a function of temperature and composition, in terms of the Warren-Cowley short-range order (SRO) parameters and effective chemical pairwise interactions. In addition to compositions close to the known binary intermetallic phases like $CrNi_2$, FeNi, $FeNi_3$ and $FeNi_8$, pronounced chemical order is found in fcc alloys near the centre of the ternary alloy composition triangle. The SRO parameter characterizing pairs of Fe and Ni atoms decreases as a function of Cr concentration. The calculated SRO parameters are compared to the available experimental data on binary and ternary alloys, and good agreement is found. Finite temperature *magnetic* properties of fcc Fe-Cr-Ni alloys are investigated using an MCE Hamiltonian constructed using a DFT database of energies and magnetic moments. MCE simulations show that ordered ternary Fe_2CrNi alloy phase remains magnetic up to fairly high temperatures due to anti-ferromagnetic coupling between (Fe,Ni) and Cr atoms in the ternary Fe-Cr-Ni matrix.

PACS numbers: 05.10.Ln, 64.60.Cn, 71.15.Mb, 75.50.Bb, 81.30.Bx

I. INTRODUCTION

Fe-Cr-Ni alloys are one of the most studied ternary alloy systems. Their significance stems from the fact that they form the basis for many types of austenitic, ferritic and martensitic steels. Ternary Fe-Cr-Ni and binary Fe-Cr, Fe-Ni and Ni-Cr alloys exhibit diverse magnetic, thermodynamic and mechanical properties, which make them suitable for a variety of applications. The alloy family includes several outstanding examples, like Invar[1] and Permalloy[2]. Fe-Cr-Ni based steels, including austenitic 304 and 316 steels, are widely used as structural materials for light water and fast breeder fission reactors[3,4]. Inconel alloys X-750 and 718 are used in reactor core components[5]. Fe-Cr-based steels F82H and Eurofer are among candidate structural materials for tritium breeding blankets of fusion reactors[6]. Since the stability of materials in extreme conditions is affected by many factors, extensive and accurate knowledge of how materials respond to temperature and irradiation over prolonged periods of time is required. The selection of optimal alloy compositions is therefore one of the objectives of fission and fusion materials research. For example, it is known that bcc alloys, like V-Cr-Ti alloys or ferritic steels, exhibit good resistance to radiation swelling. On the other hand, even in fcc $Fe_{85-x}Cr_{15}Ni_x$ (x=15, 20, 25, 30) alloys irradiated up to 6 dpa, voids still do not form above 350°C if the concentration of Ni is close to 30%[7].

Because of the broad range of applications of Fe-Cr-Ni alloys, their phase diagram has been extensively assessed from the thermodynamic perspective. Microstructure of Fe-Cr-Ni steels is well described by the Schaeffler diagram[8]. The phase composition of steels can be controlled by varying Cr and Ni content, since chromium is a ferrite (bcc phase) stabilizer and nickel is an austenite (fcc phase) stabiliser. A thermodynamic model for Fe-Cr-Ni alloys has been developed using the CALPHAD methodology, which is based on interpolation of elevated temperature experimental data[9–11]. Because of the relatively slow kinetics of relaxation towards equilibrium at low temperatures, experimental information about the low temperature part of the phase diagram is limited. This information can instead be derived from *ab initio* density functional theory (DFT) simulations[12], as it was recently done for binary Fe-Ni alloys in Ref. 13. A recent revision of Fe-Cr-Ni CALPHAD phase diagram is given in Ref. 14, where both magnetic and chemical ordering temperatures of binary Fe-Ni alloys were extrapolated to ternary alloys.

There have been only a few DFT studies of Fe-Cr-Ni ternary alloys. Properties of the alloys in the dilute Cr and Ni limit were analyzed in Refs. 15 and 16. Coherent potential approximation (CPA) was used by the authors of Refs. 17–19. Recently[20], special quasi-random structures (SQS)[21] were employed to investigate point defects in fcc $Fe_{70}Cr_{20}Ni_{10}$ alloys. In all these studies, Fe-Cr-Ni alloys were assumed to be fully chemically disordered. This assumption is in fact too strong and often unrealistic, since there is direct experimental evidence showing that short-range order is present in many Fe-Cr-Ni alloys[22–24]. Whilst chemical SRO is naturally expected for ternary alloy compositions close to the known binary intermetallic phases, for example $FeNi_3$, FeNi and $CrNi_2$, SRO in $FeNi_3$ alloyed with Cr is found to decrease rapidly as a function of Cr content[25]. Unexpectedly, significant degree of chemical order is observed in alloys with compositions very different from that of binary intermetallic phases, for example in $Fe_{56}Cr_{21}Ni_{23}$[23], $Fe_{64}Cr_{16}Ni_{20}$, $Fe_{59}Cr_{16}Ni_{25}$[22] and $Fe_{34}Ni_{46}Cr_{20}$[24].

Chemical order in alloys, and properties of ordered alloys, can be analysed using a combination of first-principles calculations and statistical mechanics simulations based on a generalization of the Ising alloy model. In the Cluster Expansion (CE) model, the energy of an alloy is represented by a series expansion in the cluster functions, and the resulting expression has the form of a generalized Ising Hamiltonian containing several coupling parameters known as effective cluster interactions (ECIs)[26]. Various methods have been developed to compute ECIs from first principles. The most often used is the structure inversion method (SIM), based on the Connolly-Williams approximation[27], and the coherent potential approximation used in combination with generalized perturbation method (CPA-GPM). In the CPA-GPM scheme, random alloy is constructed by considering average occupancies of lattice sites by atoms of alloy components, where the coupling parameters are computed using a perturbation approach[28]. In SIM, energies of ordered structures are computed using DFT, and then ECIs are obtained through least-squares fitting. Both techniques have been successfully applied to binary alloy sub-systems of Fe-Cr-Ni[28–35], but they have not been applied to the ternary Fe-Cr-Ni alloys themselves.

In this work we use SIM, since the accuracy of ECIs is primarily controlled by the approximations involved in *ab initio* calculations of energies of input structures, and by the cross-validation error between DFT and CE. The last but not least critical issue to consider is the variety of magnetic configurations characterizing fcc and bcc Fe-Cr-Ni alloys. For example, fcc $Fe_{80-x}Ni_xCr_{20}$ alloys ($10 < x < 30$) exhibit ferromagnetic, anti-ferromagnetic, or spin-glass magnetic order, or a mixture of the above[36]. To find the most stable atomic structures needed for parametrizing the CE model, many magnetic configurations were investigated and compared. Variation of magnetic properties as functions of alloy composition was investigated, including the magneto-volume effects in Fe-Cr-Ni alloys.

Effective cluster interaction parameters, obtained by mapping DFT energies of stable collinear magnetic configurations to CE, are used in quasi-canonical Monte Carlo simulations. Here we investigate phase stability and chemical order in fcc and bcc Fe-Cr-Ni alloys at finite temperatures and generate representative alloy structures for future DFT analysis of radiation defects in alloys. We also analyze magnetic properties of Fe-Cr-Ni alloys at low and high

temperatures using Magnetic Cluster Expansion-based Monte Carlo simulations.

The structure of the paper is as follows. In Section II, we describe CE formalism for multi-component alloys, focusing on ternary alloy systems, and derive short range order parameters from the cluster functions. In Section III we analyze phase stability and magnetic properties of structures obtained using DFT at 0 K. Phase stability and chemical order in alloys at finite temperatures are investigated using quasi-canonical Monte Carlo simulations in Section IV. Finite-temperature magnetic properties are explored by Magnetic Cluster Expansion simulations in Sections V. We conclude in Section VI.

II. COMPUTATIONAL METHODOLOGY

A. Cluster expansion formalism for ternary alloys

Phase stability of ternary alloys can be investigated using a combination of quantum-mechanical density-functional theory (DFT) calculations and lattice statistical mechanics simulations. The enthalpy of mixing of an alloy, which can be evaluated using DFT, is defined as

$$\begin{aligned}\Delta H^{lat}_{DFT}(\vec{\sigma}) = E^{lat}_{tot}(A_{c_B}B_{c_B}C_{c_C},\vec{\sigma}) - c_A E^{lat}_{tot}(A) \\ - c_B E^{lat}_{tot}(B) - c_C E^{lat}_{tot}(C),\end{aligned} \tag{1}$$

where c_A, c_B and c_C are the average concentrations of components A, B and C. E^{lat}_{tot} are the total energies of relevant structures defined on a chosen crystal lattice. Superscript *lat* denotes the chosen lattice type: face-centred cubic, fcc or body-centred cubic, bcc. An atomic alloy configuration is specified by a vector of configurational variables $\vec{\sigma}$.

Within cluster expansion (CE) the configurational enthalpy of mixing of a ternary alloy is[37]

$$\Delta H_{CE}(\vec{\sigma}) = \sum_{\omega} m_\omega J_\omega \left\langle \Gamma_{\omega'}(\vec{\sigma}) \right\rangle_\omega , \tag{2}$$

where summation is performed over all the clusters ω that are distinct under group symmetry operations of the underlying lattice, m^{lat}_ω are multiplicities indicating the number of clusters equivalent to ω by symmetry (divided by the number of lattice sites), $\langle\Gamma_{\omega'}(\vec{\sigma})\rangle$ are the cluster functions defined as products of *functions* of occupation variables on a specific cluster ω averaged over all the clusters ω' that are equivalent by symmetry to cluster ω. J_ω are the concentration-independent effective cluster interaction (ECI) parameters, derived from a set of *ab-initio* calculations using the structure inversion method[27].

Cluster ω is defined by its size (number of lattice points) $|\omega|$, and the relative position of points. Coordinates of points in each cluster considered here for fcc and bcc lattices are listed in Table I. For clarity, each cluster ω is described by two parameters $(|\omega|, n)$, where $|\omega|$ is the cluster size and n is a label, defined in Table I.

In binary alloys, lattice site occupation variables are usually defined as $\sigma_i = \pm 1$, where σ shows if site i is occupied by an atom of type A ($\sigma_i = +1$) or B ($\sigma_i = -1$). In this case the cluster function is defined as a product of occupation variables over all the sites included in cluster ω

$$\Gamma_{\omega,n}(\vec{\sigma}) = \sigma_1\sigma_2\ldots\sigma_{|\omega|}. \tag{3}$$

In K-component systems, a cluster function is not a simple product of occupation variables, and is instead defined as a product of orthogonal point functions $\gamma_{j_i,K}(\sigma_i)$,

$$\Gamma^{(s)}_{\omega,n}(\vec{\sigma}) = \gamma_{j_1,K}(\sigma_1)\gamma_{j_2,K}(\sigma_2)\ldots\gamma_{j_{|\omega|},K}(\sigma_{|\omega|}), \tag{4}$$

where sequence $(s) = (j_1 j_2 \ldots\ j_{|\omega|})$ is the *decoration*[38] of cluster by point functions. All the decorations of clusters, which are not symmetry-equivalent for fcc and/or bcc ternary alloys, are presented in Table I together with their multiplicities $m^{(s)}_{|\omega|,n}$ and effective cluster interactions $J^{(s)}_{|\omega|,n}$.

The number of possible decorations of clusters by non-zero point functions is a permutation with repetitions, $(K-1)^{|\omega|}$. Effective cluster interactions for those clusters are given in Table I only once, together with the corresponding multiplicity factor $m_{|\omega|,n}$. In ternary alloys, occupation variables and point functions can be defined in different ways. For example, in Ref. 26 and 39 occupation variables are defined as $\sigma_i = -1, 0, +1$ and point functions as: $\gamma_{0,3} = 1$ (for the zero cluster), $\gamma_{1,3}(\sigma_i) = \sqrt{\frac{3}{2}}\sigma_i$, and $\gamma_{2,3}(\sigma_i) = \sqrt{2}(1 - \frac{3}{2}\sigma_i^2)$.

In this work, occupation variables and point functions are defined as in Ref. 37, making it possible to use the same formulae as for a K-component system

$$\gamma_{j,K}\left(\sigma_i\right) = \begin{cases} 1 & \text{if } j = 0\ , \\ -\cos\left(2\pi\lceil\frac{j}{2}\rceil\frac{\sigma_i}{K}\right) & \text{if } j > 0 \text{ and odd}, \\ -\sin\left(2\pi\lceil\frac{j}{2}\rceil\frac{\sigma_i}{K}\right) & \text{if } j > 0 \text{ and even}, \end{cases} \tag{5}$$

where $\sigma_i = 0, 1, 2, \ldots, (K-1)$, j is the index of point functions ($j = 0, 1, 2, \ldots, (K-1)$), and $\lceil\frac{j}{2}\rceil$ denotes an operation where we take the integer plus one value of a non-integer number, for example $\lceil 2.5\rceil = 3$. In ternary alloys, index K equals 3, and in what follows it will be dropped to simplify notations. Occupation variables are now defined as $\sigma = 0, 1, 2$, indicating the constituting components of the alloy A, B and C, which here correspond to Fe, Cr, and Ni, respectively.

The enthalpy of mixing (Eq. 2) of a ternary alloy on a lattice can now be written as

$$\begin{aligned} \Delta H_{CE}(\vec{\sigma}) &= \sum_{|\omega|,n,s} m^{(s)}_{|\omega|,n} J^{(s)}_{|\omega|,n} \left\langle \Gamma^{(s')}_{|\omega'|,n'}(\vec{\sigma}) \right\rangle_{|\omega|,n,s} \\ &= J^{(0)}_{1,1}\left\langle \Gamma^{(0)}_{1,1}\right\rangle + J^{(1)}_{1,1}\left\langle \Gamma^{(1)}_{1,1}\right\rangle + J^{(2)}_{1,1}\left\langle \Gamma^{(2)}_{1,1}\right\rangle + \sum_{n=1}^{pairs}\Big(m^{(11)}_{2,n}J^{(11)}_{2,n}\left\langle \Gamma^{(11)}_{2,n}\right\rangle + m^{(12)}_{2,n}J^{(12)}_{2,n}\left\langle \Gamma^{(12)}_{2,n}\right\rangle \\ &+ m^{(22)}_{2,n}J^{(22)}_{2,n}\left\langle \Gamma^{(22)}_{2,n}\right\rangle\Big) + \sum_{n=1}^{multibody} \ldots \end{aligned} \tag{6}$$

The relevant expressions for fcc and bcc alloys differ because of different multiplicity factors, $m^{(s)}_{|\omega|,n}$, given in Table I.

TABLE I. Size $|\omega|$, label n, decoration (s), multiplicity $m^{(s)}_{|\omega|,n}$ and coordinates of points in the relevant clusters on fcc and bcc lattices. $J^{(s)}_{|\omega|,n}$ (in meV) are the effective cluster interaction parameters for fcc and bcc ternary Fe-Cr-Ni alloys. Index (s) is the same as the sequence of points in the relevant cluster.

			fcc			bcc		
$\|\omega\|$	n	(s)	Coordinates	$m^{(s)}_{\|\omega\|,n}$	$J^{(s)}_{\|\omega\|,n}$	Coordinates	$m^{(s)}_{\|\omega\|,n}$	$J^{(s)}_{\|\omega\|,n}$
1	1	(0)	(0,0,0)	1	-77.281	(0,0,0)	1	132.945
		(1)		1	-60.747		1	47.929
		(2)		1	2.847		1	-168.929
2	1	(1,1)	(0,0,0; $\frac{1}{2},\frac{1}{2}$,0)	6	4.329	(0,0,0; $\frac{1}{2},\frac{1}{2},\frac{1}{2}$)	4	-54.656
		(1,2)		12	-2.057		8	-4.140
		(2,2)		6	-2.039		4	-64.784
2	2	(1,1)	(0,0,0; 1,0,0)	3	-9.596	(0,0,0; 1,0,0)	3	-19.159
		(1,2)		6	7.284		6	7.332
		(2,2)		3	-31.827		3	-19.253
2	3	(1,1)	(0,0,0; 1,$\frac{1}{2},\frac{1}{2}$)	12	3.345	(0,0,0; 1,0,1)	6	-1.547
		(1,2)		24	-0.702		12	11.871
		(2,2)		12	4.224		6	8.392
2	4	(1,1)	(0,0,0; 1,1,0)	6	-1.990	(0,0,0; $1\frac{1}{2},\frac{1}{2},\frac{1}{2}$)	12	2.466
		(1,2)		12	1.192		24	0.564
		(2,2)		6	6.662		12	-2.660
2	5	(1,1)	(0,0,0; $1\frac{1}{2},\frac{1}{2},\frac{1}{2}$)	6	-2.034	(0,0,0; 1,1,1)	4	1.602
		(1,2)		12	0.724		8	-1.368
		(2,2)		6	2.036		4	3.031
3	1	(1,1,1)	(0,0,0; $\frac{1}{2}$,0,$\frac{1}{2}$;	8	-9.015	(1,0,0; $\frac{1}{2},\frac{1}{2},\frac{1}{2}$;	12	-6.961
		(2,1,1)	0,$\frac{1}{2},\frac{1}{2}$)	24	3.847	0,0,0)	24	8.827
		(1,2,1)					12	1.620
		(2,2,1)		24	-6.544		24	-1.954
		(2,1,2)					12	22.895
		(2,2,2)		8	12.492		12	2.934

TABLE I. (*Continued*)

			fcc			bcc		
$\|\omega\|$	n	(s)	Coordinates	$m^{(s)}_{\|\omega\|,n}$	$J^{(s)}_{\|\omega\|,n}$	Coordinates	$m^{(s)}_{\|\omega\|,n}$	$J^{(s)}_{\|\omega\|,n}$
3	2	(1,1,1)	(1,0,0; $\frac{1}{2}$,-$\frac{1}{2}$,0;	12	-3.019	($\frac{1}{2}$,-$\frac{1}{2}$,-$\frac{1}{2}$; 0,0,0;	12	-6.255
		(2,1,1)	0,0,0)	24	-0.470	-$\frac{1}{2}$,-$\frac{1}{2}$,$\frac{1}{2}$)	24	2.510
		(1,2,1)		12	-1.778		12	-1.292
		(2,2,1)		24	5.371		24	6.122
		(2,1,2)		12	6.310		12	6.580
		(2,2,2)		12	-0.126		12	4.334
3	3	(1,1,1)	($\frac{1}{2}$,$\frac{1}{2}$,0; 0,0,0;	24	0.821			
		(2,1,1)	-$\frac{1}{2}$,0,$\frac{1}{2}$)	48	-0.017			
		(1,2,1)		24	0.931			
		(2,2,1)		48	0.369			
		(2,1,2)		24	2.657			
		(2,2,2)		24	-3.945			
4	1	(1,1,1,1)	(0,0,0; $\frac{1}{2}$,$\frac{1}{2}$,0;	2	-12.978	(1,0,0; $\frac{1}{2}$,-$\frac{1}{2}$,$\frac{1}{2}$;	6	-12.095
		(2,1,1,1)	$\frac{1}{2}$,0,$\frac{1}{2}$; 0,$\frac{1}{2}$,$\frac{1}{2}$)	8	-1.931	$\frac{1}{2}$,$\frac{1}{2}$,$\frac{1}{2}$; 0,0,0)	24	-13.020
		(2,2,1,1)		12	4.987		24	0.000
		(1,2,2,1)					12	0.000
		(2,2,2,1)		8	-1.140		24	0.000
		(2,2,2,2)		2	0.824		6	0.007
4	2	(1,1,1,1)	(1,0,0; $\frac{1}{2}$,0,$\frac{1}{2}$;	12	-1.452			
		(2,1,1,1)	$\frac{1}{2}$,-$\frac{1}{2}$,0; 0,0,0)	24	1.076			
		(1,2,1,1)		24	-1.775			
		(2,2,1,1)		48	1.114			
		(1,2,2,1)		12	-0.581			
		(2,2,2,1)		24	-5.109			
		(2,1,1,2)		12	4.130			
		(2,2,1,2)		24	2.549			
		(2,2,2,2)		12	6.127			
5	1	(1,1,1,1,1)	(1,0,0; $\frac{1}{2}$,0,-$\frac{1}{2}$;	6	4.219	(1,0,0; $\frac{1}{2}$,-$\frac{1}{2}$,$\frac{1}{2}$;	12	-6.356
		(2,1,1,1,1)	$\frac{1}{2}$,0,$\frac{1}{2}$; $\frac{1}{2}$,-$\frac{1}{2}$,0;	24	-1.263	$\frac{1}{2}$,$\frac{1}{2}$,$\frac{1}{2}$; 0,0,0)	24	7.696
		(1,2,1,1,1)	0,0,0)			0,0,1)	24	-15.998
		(2,2,1,1,1)		24	0.626		48	15.385
		(1,2,2,1,1)		12	1.676		12	-20.341
		(2,2,2,1,1)		24	-0.360		24	14.846
		(1,1,1,2,1)		6	-6.115		12	-5.003
		(2,1,1,2,1)		24	-1.565		24	-3.067
		(1,2,1,2,1)					24	-3.221
		(2,2,1,2,1)		24	3.258		48	1.070
		(1,2,2,2,1)		12	2.284		12	-3.473
		(2,2,2,2,1)		24	-1.400		24	-1.255
		(2,1,1,1,2)					12	11.683
		(2,2,1,1,2)					24	-1.192
		(2,2,2,1,2)		6	1.565		12	-2.460
		(2,1,1,2,2)					12	-6.855
		(2,2,1,2,2)					24	-7.050
		(2,2,2,2,2)		6	-6.793		12	-5.397

Configuration averages $\left\langle \Gamma^{(s)}_{|\omega|,n}(\vec{\sigma}) \right\rangle$ in Eq. 6 can be expressed in terms of point, pair and multi-body probabilities. An average point correlation function can be calculated using the formula

$$\left\langle \Gamma^{(s)}_{1,1} \right\rangle = \langle \gamma_j \rangle = \sum_{k=1}^{3} T_{jk} \times \langle p^{(k)} \rangle = \sum_{k=1}^{3} T_{jk} c_k, \tag{7}$$

where $k = 0, 1, 2$, $p^{(k)}$ are site-occupation operators counting the number of sites occupied by the same atom type[40]. Average values of site-occupation operators $\left\langle p^{(k)} \right\rangle = c_k$ are the concentrations c_A, c_B and c_C, respectively, and T_{ij}

are the elements of point probability matrix that are given, via Eq. 5, by

$$\begin{bmatrix} \langle\gamma_0\rangle \\ \langle\gamma_1\rangle \\ \langle\gamma_2\rangle \end{bmatrix} = \begin{bmatrix} 1 & 1 & 1 \\ -1 & \frac{1}{2} & \frac{1}{2} \\ 0 & -\frac{\sqrt{3}}{2} & \frac{\sqrt{3}}{2} \end{bmatrix} \begin{bmatrix} \langle p^{(0)}\rangle \\ \langle p^{(1)}\rangle \\ \langle p^{(2)}\rangle \end{bmatrix}. \tag{8}$$

The three average point functions are therefore

$$\begin{aligned} \left\langle \Gamma^{(0)}_{1,1} \right\rangle &= \langle\gamma_0\rangle = \sum_i c_i \gamma_0(\sigma_i) = 1 \\ \left\langle \Gamma^{(1)}_{1,1} \right\rangle &= \langle\gamma_1\rangle = \sum_i c_i \gamma_1(\sigma_i) = \frac{1}{2}\left(-2c_A + c_B + c_C\right) = \frac{1}{2}\left(1 - 3c_A\right) \\ \left\langle \Gamma^{(2)}_{1,1} \right\rangle &= \langle\gamma_2\rangle = \sum_i c_i \gamma_2(\sigma_i) = \frac{\sqrt{3}}{2}\left(c_C - c_B\right). \end{aligned} \tag{9}$$

Similarly to Eq. 7, the average cluster functions for pair clusters (n-th nearest neighbours) are linear functions of the average pair probabilities. They are given by

$$\begin{aligned} \left\langle \Gamma^{(ij)}_{2,n} \right\rangle &= \langle\gamma_i, \gamma_j\rangle_n = \sum_{h=1}^{3}\sum_{k=1}^{3} T_{ih}T_{jk} \times \langle p^{(h)}p^{(k)}\rangle_n \\ &= \sum_{h=1}^{3}\sum_{k=1}^{3} \gamma_i(\sigma_h)\gamma_j(\sigma_k) y_n^{hk}, \end{aligned} \tag{10}$$

where T_{ih} and T_{jk} are elements of the point probability matrix (Eq. 8), and y_n^{hk} is the temperature dependent probability of finding atom h near atom k in the n-th nearest neighbour coordination shell, given by[40]

$$y_n^{hk} = \langle p^{(h)}p^{(k)}\rangle_n = \langle p^{(h)}\rangle\langle p^{(k)}\rangle\left(1 - \alpha_n^{hk}\right) = c_h c_k\left(1 - \alpha_n^{hk}\right). \tag{11}$$

Here α_n^{hk} is the Warren-Cowley short-range parameter for atoms h and k in the n-th neighbour shell, defined as the deviation from the fully random distribution of atoms in the alloy. Average cluster functions for the three pairs of non-equivalent atoms are therefore

$$\begin{aligned} \left\langle \Gamma^{(11)}_{2,n} \right\rangle &= \langle\gamma_1, \gamma_1\rangle_n = \\ &= \frac{1}{4}\left(1 + 3y_n^{AA} - 6y_n^{AB} - 6y_n^{AC}\right) \\ \left\langle \Gamma^{(12)}_{2,n} \right\rangle &= \langle\gamma_1, \gamma_2\rangle_n = \\ &= \frac{\sqrt{3}}{4}\left(-y_n^{BB} + y_n^{CC} + 2y_n^{AB} - 2y_n^{AC}\right) \\ \left\langle \Gamma^{(22)}_{2,n} \right\rangle &= \langle\gamma_2, \gamma_2\rangle_n = \frac{3}{4}\left(y_n^{BB} + y_n^{CC} - 2y_n^{BC}\right). \end{aligned} \tag{12}$$

Rewriting Eq. 6 in terms of average point and pair functions given by Eqs. 9 and 12, respectively, we arrive at that the configurational enthalpy of mixing for a ternary alloy can now be expressed as a function of concentrations c_i, and average pair probabilities y_n^{ij}, namely

$$\begin{aligned} \Delta H_{CE}(\vec{\sigma}) = {} & J_1^{(0)} + J_1^{(1)}\left(1 - 3c_A\right) + J_1^{(2)}\frac{\sqrt{3}}{2}\left(c_C - c_B\right) \\ & + \sum_n^{pairs}\left[\frac{1}{4}m_{2,n}^{(11)}J_{2,n}^{(11)}\left(1 + 3y_n^{AA} - 6y_n^{AB} - 6y_n^{AC}\right) + \frac{\sqrt{3}}{4}m_{2,n}^{(12)}J_{2,n}^{(12)}\left(-y_n^{BB} + y_n^{CC} + 2y_n^{AB} - 2y_n^{AC}\right)\right. \\ & \left. + \frac{3}{4}m_{2,n}^{(22)}J_{2,n}^{(22)}\left(y_n^{BB} + y_n^{CC} - 2y_n^{BC}\right)\right] + \sum_n^{multibody} \ldots \end{aligned} \tag{13}$$

Detailed expressions, with analytic formulae, for the average cluster functions of 3-body clusters as well as for the enthalpy of mixing represented as a function of average triple probabilities y_n^{ijk}, are given in Appendix A.

B. Chemical short-range order parameters

Short-range order in ternary alloys can be investigated by analyzing chemical pairwise interactions between the unlike atoms. These pairwise interactions are related to $J^{(s)}_{|\omega|,n}$, where $|\omega| = 2$ and $J^{(s)}_{|\omega|,n}$ are given by an inner product of a cluster function $\Gamma^{(s)}_{2,n}$ and the corresponding energy[39,41], namely

$$J^{(s)}_{2,n} = \langle \Gamma^{(s)}_{2,n}(\vec{\sigma}), E(\vec{\sigma}) \rangle = \rho^{(s)}_0 \sum_{\{\vec{\sigma}\}} \Gamma^{(s)}_{2,n}(\vec{\sigma}) E(\vec{\sigma}). \tag{14}$$

Summation in the above equation is performed over all possible configurations and $\rho^{(s)}_0$ is a normalization constant chosen to satisfy the orthonormality criterion for cluster functions $\Gamma^{(s)}_{2,n}$. Effective cluster interactions in ternary alloys for pairs of non-zero point functions with indices (11),(12),(21) and (22) can now be written as

$$J^{(ij)}_{2,n} = \frac{4}{9} \sum_{h,k} E^{hk}_n \gamma_i(\sigma_h) \gamma_j(\sigma_k). \tag{15}$$

where E^{hk}_n is the average energy of configurations with atom h being in the n-th nearest neighbour shell of atom k. From Eq. 15, ECI for pairs with indices (11),(12),(21) and (22) are

$$\begin{aligned}
J^{(11)}_{2,n} &= \frac{1}{9} \left(4E^{AA}_n + E^{BB}_n + E^{CC}_n - 2E^{AB}_n - 2E^{BA}_n \right. \\
&- \left. 2E^{AC}_n - 2E^{CA}_n + E^{BC}_n + E^{CB}_n \right), \\
J^{(12)}_{2,n} &= \frac{1}{2} \left(J^{(12)}_{2,n} + J^{(21)}_{2,n} \right) = \frac{\sqrt{3}}{9} \left(-E^{BB}_n + E^{CC}_n \right. \\
&+ \left. E^{AB}_n + E^{BA}_n - E^{AC}_n - E^{CA}_n \right) \\
J^{(22)}_{2,n} &= \frac{1}{3} \left(E^{BB}_n + E^{CC}_n - E^{BC}_n - E^{CB}_n \right).
\end{aligned} \tag{16}$$

Chemical pairwise interaction between atoms i and j in the n-th neighbour shell in a ternary alloy is defined as the effective cluster interaction between pairwise clusters in binary alloys[39,41]

$$V^{ij}_n = \frac{1}{4} \left(E^{ii}_n + E^{jj}_n - E^{ij}_n - E^{ji}_n \right), \tag{17}$$

where energies E^{ii}_n, E^{jj}_n, E^{ij}_n and E^{ji}_n are averaged over all the ternary configurations. From Eqs. 16 and 17, a relation between chemical pairwise interactions between the unlike atoms and effective cluster interactions of pairwise clusters in a ternary alloy can be written in a matrix form as

$$\begin{bmatrix} V^{AB}_n \\ V^{AC}_n \\ V^{BC}_n \end{bmatrix} = \begin{bmatrix} \frac{9}{16} & \frac{-3\sqrt{3}}{8} & \frac{3}{16} \\ \frac{9}{16} & \frac{3\sqrt{3}}{8} & \frac{3}{16} \\ 0 & 0 & \frac{3}{4} \end{bmatrix} \begin{bmatrix} J^{(11)}_{2,n} \\ J^{(12)}_{2,n} \\ J^{(22)}_{2,n} \end{bmatrix}. \tag{18}$$

Like in a binary alloy case, chemical pairwise interactions V^{ij}_n have a simple meaning: $V^{ij}_n > 0$ corresponds to attraction and $V^{ij}_n < 0$ to repulsion between atoms i and j. These interactions will be used in the analysis of SRO in Fe-Cr-Ni ternary alloys in Section IV.C. With Eq. 13 expressed in terms of chemical pairwise interactions, the configurational enthalpy of mixing of a ternary alloy is given by

$$\begin{aligned}
\Delta H_{CE}(\vec{\sigma}) &= J^{(0)}_1 + J^{(1)}_1 (1 - 3c_A) + J^{(2)}_1 \frac{\sqrt{3}}{2} (c_C - c_B) \\
&- 4 \sum_n^{pairs} \left(V^{AB}_n y^{AB}_n + V^{AC}_n y^{AC}_n + V^{BC}_n y^{BC}_n \right) + \sum_n^{multibody} \ldots,
\end{aligned} \tag{19}$$

The degree of SRO between atoms i and j in the n-th nearest neighbour shell in both binary and ternary alloys can be described using the Warren-Cowley parameters α^{ij}_n used in Eq. 11

$$\alpha^{ij}_n = 1 - \frac{\langle p^{(i)}, p^{(j)} \rangle_n}{\langle p^{(i)} \rangle \langle p^{(j)} \rangle} = 1 - \frac{y^{ij}_n}{c_i c_j} = 1 - \frac{P^{i-j}_n}{1 - c_i}. \tag{20}$$

Here n is a coordination sphere index, c_i and c_j are the concentrations of i's and j's atoms, respectively, and $P_n^{i-j} = y_n^{ij}/c_i$ is the conditional probability of finding atom i in the n-th coordination sphere of atom j, see for example Ref[42]. Like in the binary alloy case, α_n^{ij} vanishes if $P_n^{i-j} = c_j$, meaning that there is no preference for a given atom to be surrounded by atoms of any other type (an ideal solid solution). Segregation gives rise to positive α_n^{ij}, whereas negative values indicate ordering. If at low concentration of atoms j each atom j is surrounded by i atoms only ($P_n^{i-j} = 1$) then α_n^{ij} takes its lowest possible value $\alpha_{n,min}^{ij} = -(1 - c_i)/c_i$.

SRO parameters can be expressed in terms of average point and pair correlation functions. Inverting Eqs. 8, 10 and Eq. 20, analytic formulae for SRO parameters in a ternary alloy acquire the form

$$\begin{aligned}
\alpha_n^{AB} &= 1 - \frac{2 - 2\langle\gamma_1\rangle - 2\sqrt{3}\langle\gamma_2\rangle - 4\langle\gamma_1,\gamma_1\rangle_n + 4\sqrt{3}\langle\gamma_1,\gamma_2\rangle_n}{2(1 - 2\langle\gamma_1\rangle)(1 + \langle\gamma_1\rangle - \sqrt{3}\langle\gamma_2\rangle)} \\
\alpha_n^{BC} &= 1 - \frac{2 + 4\langle\gamma_1\rangle + 2\langle\gamma_1,\gamma_1\rangle_n - 6\langle\gamma_2,\gamma_2\rangle_n}{2(1 + \langle\gamma_1\rangle - \sqrt{3}\langle\gamma_2\rangle)(1 + \langle\gamma_1\rangle + \sqrt{3}\langle\gamma_2\rangle)} \\
\alpha_n^{AC} &= 1 - \frac{2 - 2\langle\gamma_1\rangle + 2\sqrt{3}\langle\gamma_2\rangle - 4\langle\gamma_1,\gamma_1\rangle_n - 4\sqrt{3}\langle\gamma_1,\gamma_2\rangle_n}{2(1 - 2\langle\gamma_1\rangle)(1 + \langle\gamma_1\rangle + \sqrt{3}\langle\gamma_2\rangle)}.
\end{aligned} \tag{21}$$

Since both point and pair correlation functions are generated by the ATAT package[43] used in the present study, the SRO parameters of ternary alloys are going to be calculated using Eq. 21.

C. Computational details

DFT calculations were performed using the projector augmented wave (PAW) method implemented in VASP[44,45]. Exchange and correlation were treated in the generalized gradient approximation GGA-PBE[46]. To accelerate DFT calculations, we used PAW potentials without semi-core p electron contribution. The core configurations of Fe, Cr and Ni in PAW potentials were [Ar]3d^{7}4s^1, [Ar]3d^{5}4s^1 and [Ar]3d^{9}4s^1, respectively.

Total energies were calculated using the Monkhorst-Pack mesh[47] of k-points in the Brillouin zone, with k-mesh spacing of 0.2 $\mathring{A}^{-1}$. This corresponds to 14×14×14 or 12×12×12 k-point meshes for a two-atom bcc cubic cell or a four-atom fcc cubic cell, respectively. The plane wave cut-off energy used in the calculations was 400 eV. Total energy convergence criterion was set to 10^{-6} eV/cell and force components were relaxed to 10^{-3} eV/$\mathring{A}$.

Mapping of DFT energies to CE was performed using the ATAT package[43]. In order to find CE parameters for binary fcc alloys we used the database of 28 structures from Table I of Ref. 48. For binary bcc alloys we use 58 structures from Table I of Ref. 30. For ternary fcc alloys we used 98 structures from Fig. 2 of Ref. 49. To our knowledge, no database of structures of bcc ternary alloys is presently available. We constructed input ternary bcc structures using binary structures of Ref. 30 as a starting point. The symmetry and the number of non-equivalent positions (NEPs) in each structure was checked, and structures for which the number of NEPs was greater than two were included into the ternary bcc structure database. The resulting input database for bcc ternary alloys consists of 94 structures. These structures are described in detail in Appendix B.

Most of the collinear spin-polarized DFT calculations were performed assuming that the initial magnetic moments of Fe, Cr and Ni atoms were +3, -1 and +1 μ_B, respectively. Since magnetic properties of Fe-Cr-Ni alloys are very complex in comparison with the corresponding binary alloy sub-systems, full relaxations starting with different initial magnetic configurations were performed in order to find the most stable magnetic order characterising a given structure. Such an investigation was especially critical for fcc Fe-rich structures, where the energies of competing magnetic configurations are very close.

Initial values of ECIs, derived by mapping to CE the DFT energies computed for the most stable magnetic configurations of input structures, served as a starting point for further refinement of CE parameters, which was achieved by generating new structures. The complexity of magnetic properties of Fe-Cr-Ni alloys made it impossible to perform refining fully automatically, like in the case of non-magnetic alloys. For example, the above choice of initial values of magnetic moments did not always lead to the most stable magnetic configurations. Hence results had to be filtered as was proposed in Ref. 33. For Fe-Cr-Ni alloys it meant that some of the structures had to be recalculated assuming an alternative initial magnetic configuration or, in a few extreme cases, the less stable structures had to be eliminated if their energies proved difficult to fit to a consistent set of ECIs.

Despite the fact that fully automatic refinement of CE parameters was not possible, reasonable values of cross-validation (CV) error between DFT and CE formation enthalpies were achieved, proving that the final set of ECI describes interatomic interactions in Fe-Cr-Ni system reasonably well. A detailed description of ECIs, the number of structures used in the fitting, and CV error between DFT and CE results is given in Section III.

Quasi-canonical MC simulations were performed using the ATAT package[43]. Most of the simulations were performed using a cell containing 8000 atoms in the form of 20×20×20 *primitive* fcc or bcc unit cells. For each composition, simulations were performed starting from a disordered high-temperature state (usually $T = 2500$ K) and the system was then cooled down with the temperature step of $\Delta T = 100$K, with 5000 Monte Carlo steps per atom at both thermalization and accumulation stages. Test were conducted with 3000 and 5000 Monte Carlo steps at each of these stages. Since the results were not significantly different, the number of steps was not increased further.

A database of enthalpies of mixing and magnetic moments of ternary fcc Fe-Cr-Ni structures derived from DFT and used for fitting the Magnetic Cluster Expansion Hamiltonian (see Section V) is given in Supplementary Material Part 1.

III. PHASE STABILITY AND MAGNETIC PROPERTIES AT 0 K

A. Pure Elements

Magnetism of Fe-Cr-Ni alloys gives rise to several structural and magnetic instabilities. This effect is well known in pure iron. *Ab initio* analysis of structural and magnetic phase stability of iron was performed in Refs. 50 and 51. Our calculations confirm that the most stable Fe phase at 0 K is ferromagnetic (FM) bcc. Anti-ferromagnetic single layer (AFMSL) and anti-ferromagnetic double layer (AFMDL) fcc structures are more stable than the high-spin (HS) and low-spin (LS) ferromagnetic configurations. We extend analysis of anti-ferromagnetism in iron to the anti-ferromagnetic triple layer (AFMTL) fcc and bcc structure. We predict that fcc-Fe AFMTL has the same energy per atom as fcc-Fe AFMDL but they have significantly different volumes, see Table II. Bcc Fe AFMTL structure of iron is more stable than bcc Fe AFMSL and bcc Fe AFMDL, but it is still less stable than bcc Fe FM.

DFT calculations confirm that the most stable collinear magnetic Cr and Ni phases at 0 K are anti-ferromagnetic bcc and ferromagnetic fcc. Ferromagnetic bcc Ni and non-magnetic fcc Cr are 0.096 eV/atom and 0.405 eV/atom less stable than fcc Ni and bcc Cr, respectively.

Since the ground states of Fe, Cr and Ni belong to different crystal lattices, the phase stability of Fe-Cr-Ni alloys and binary sub-systems is analyzed in terms of their enthalpy of formation, defined as the energy of the alloy, calculated at zero pressure, with respect to the energies of ferromagnetic bcc-Fe, ferromagnetic fcc-Ni, and anti-ferromagnetic bcc-Cr. To investigate the properties of alloys on fcc and bcc crystal lattices, stabilities of fcc and bcc alloys are also analyzed in terms of their enthalpy of mixing, defined as the energy of an alloy with respect to the energies of fcc or bcc structures of pure elements, where the choice of bcc or fcc depends on the choice of the crystal structure of the alloy under consideration.

B. Fe-Ni binary alloys

There is extensive literature on models for Fe-Ni alloys, see for example Refs. 33, 34, 58–63. Recently[64], we used a DFT database to investigate magnetic properties of Fe-Ni alloys by parameterizing Magnetic Cluster Expansion. In this sub-section, we compare our DFT results with previous experimental and theoretical studies, focusing on the stability of magnetic configurations and equilibrium volume of alloy structures.

Our results agree with the assertion, derived from simulations[33,58,59] and experiments[65,66], that fcc FeNi ($L1_0$), $FeNi_3$ ($L1_2$) and $FeNi_8$ (Pt_8Ti-like[33]) compounds are the global (on both fcc *and* bcc lattices) ground states for the relevant compositions, see Fig. 1(a). Our results agree with those of Ref. 33 that on fcc lattice the ferromagnetic Z1(100) phase of Fe_3Ni (see Fig. 3 in Ref. 33) is more stable than $L1_2$, as was previously thought according to Refs. 58, 61, 65, and 67.

In Ref. 33 the AFMDL configuration of fcc FeNi alloys was not investigated, despite the fact that AFMDL represents the most stable magnetic configuration of fcc-Fe, see our Table II and Refs. 15, 50, and 51. In relation to the AFMDL structure of fcc FeNi, the Z1 Fe_3Ni structure[68] is not the ground state, instead another fcc ground state, Fe_3Ni_2 with $I4/mmm$ symmetry, is predicted by CE, see Fig. 1(a). None of the AFM fcc structures are the actual ground states, however the energies of fcc Fe_5Ni AFMTL, ferri-magnetic fcc Fe_5Ni, and fcc Fe_4Ni AFMTL, are fairly close to the bottom of the zero temperature phase stability curve, and hence may affect the finite temperature stability of fcc alloys.

Our CE calculations also predict two bcc ground states, Fe_4Ni_5 (VZn-like[30]) and $FeNi_5$ (of $Cmmm$ symmetry) that are still less stable than fcc structures of similar compositions, see Figs. 1(b) and 5. Fe_4Ni_5 (VZn-like) bcc structure has the lowest energy in both DFT and CE simulations.

Enthalpies of mixing of fcc and bcc Fe-Ni structures calculated using DFT and CE are compared in Fig. 1(a,b). To remain consistent with the choice of other binary alloys Fe-Cr and Ni-Cr, we used the same sets of cluster interaction

TABLE II. Volume per atom V, energy with respect to the energy of the ground state, $E - E_{GS}$, and the size of magnetic moments per atom $|m_{tot}|$, computed for various structures of pure elements and compared with experimental data.

Struct. Name	V (Å^3/atom)	$V^{Expt.}$ (Å^3/atom)	$E - E_{GS}$ (eV)	$\|m_{tot}\|$ (μ_B)	$\|m_{tot}^{Expt.}\|$ (μ_B)
bcc-Fe (FM) -GS	11.35	11.70[52]	0.000	2.199	2.22[53]
bcc-Fe (NM)	10.46		0.475	0.000	
bcc-Fe (AFMSL)	10.87		0.444	1.290	
bcc-Fe (AFMDL)	11.34		0.163	2.104	
bcc-Fe (AFMTL)	11.35		0.112	4×2.087; 2×2.351	
fcc-Fe (NM)	10.22		0.167	0.000	
fcc-Fe (FM-HS)	11.97	12.12[52]	0.153	2.572	
fcc-Fe (FM-LS)	10.52		0.162	1.033	
fcc-Fe (AFMSL)	10.76	11.37[52]	0.100	1.574	0.75[54]
fcc-Fe (AFMDL)	11.20		0.082	2.062	
fcc-Fe (AFMTL)	11.45		0.082	8×2.155; 4×2.429	
bcc-Cr (AFMSL) -GS	11.63	11.94[55]	0.000	1.070	
bcc-Cr (NM)	11.41		0.011	0.000	
fcc-Cr (NM)	11.75		0.405	0.000	
fcc-Ni (FM) -GS	10.91	10.90[55]	0.000	0.641	0.60[53]
fcc-Ni (NM)	10.84		0.056	0.000	
bcc-Ni (FM)	11.00		0.092	0.569	
bcc-Ni (NM)	10.90		0.107	0.000	

parameters, namely five two-body, three three-body, two four-body, one five-body clusters, for fcc binary alloys and five two-body, two three-body, one four-body, one five-body clusters for the corresponding bcc alloys. A set of ECIs obtained by mapping energies of structures from DFT to CE is given in Fig. 4 and Table VIII in Appendix. The cross-validation errors between DFT and CE are 8.1 and 10.9 meV/atom for fcc and bcc Fe-Ni alloys, respectively.

The magnitude and sign of ECIs explain the behaviour of fcc and bcc Fe-Ni alloys found in simulations. In fcc alloys the first and third nearest neighbour (1NN and 3NN) pair interactions are positive whereas the second nearest neighbour (2NN) interaction is negative. In binary alloys, from Eqs. 2 and 3, this favours having the unlike atoms occupying the first and third neighbour coordination shell, and the like atoms occupying the second neighbour shell. On fcc lattice this favours the formation of the $L1_2$ intermetallic phase, which is the ground state of fcc Fe-Ni alloy. In bcc alloys the 1NN Fe-Ni pair interaction is negative, indicating repulsive interaction between the unlike atoms in the first neighbour shell. The 2NN pair interaction is positive and similar in its magnitude to the 1st ECI. As a result, bcc Fe-Ni alloys exhibit several intermetallic phases with negative enthalpies of mixing.

Atomic volumes of fcc and bcc alloys shown in Fig. 1(c,d) are not linear functions of Ni content. This non-linearity stems from the difference between atomic sizes of Fe and Ni *and* magnetism, see Fig. 1(e,f). Bcc alloys with low Ni content have larger volume per atom than pure Fe, despite the fact that Ni atoms have smaller size. This is correlated with the fact that $Fe_{15}Ni$ structure has the largest average atomic magnetic moment, 2.31 μ_B. In fcc Fe-Ni alloy the non-linearity of atomic volume as a function of Ni content is even more pronounced, since alloys with Ni content lower than 25% exhibit anti-ferromagnetic interaction between Fe and Ni, resulting in the higher atomic density than ferromagnetically ordered alloys. Experimental measurements[57] show that the atomic volume is maximum for Fe-Ni alloys with ~ 37 at. % Ni. This is also related to the fact that Fe_3Ni_2 intermetallic phase has the largest volume per atom, see Fig.1(c). There are several structures with smaller Ni content that are ferromagnetically ordered at 0K and have larger volumes per atom than Fe_3Ni_2. Those structures are metastable, and alloys with Ni concentration below 40 at. % Ni are mixtures of ferromagnetic Fe_3Ni_2, anti-ferromagnetic Fe, and metastable ferromagnetic and anti-ferromagnetic alloy phases. Near 25 at. % Ni concentration the most stable magnetic configurations are ferromagnetic, however the energy difference between them and anti-ferromagnetic phases characterized by smaller volumes is fairly small. In particular, the most stable structure corresponding to 33 at. % Ni is the ferromagnetic β-phase[33] where the enthalpy of mixing is -0.070 eV/atom and the atomic volume is 11.47 $Å^3$ per atom. The AFMTL structure is

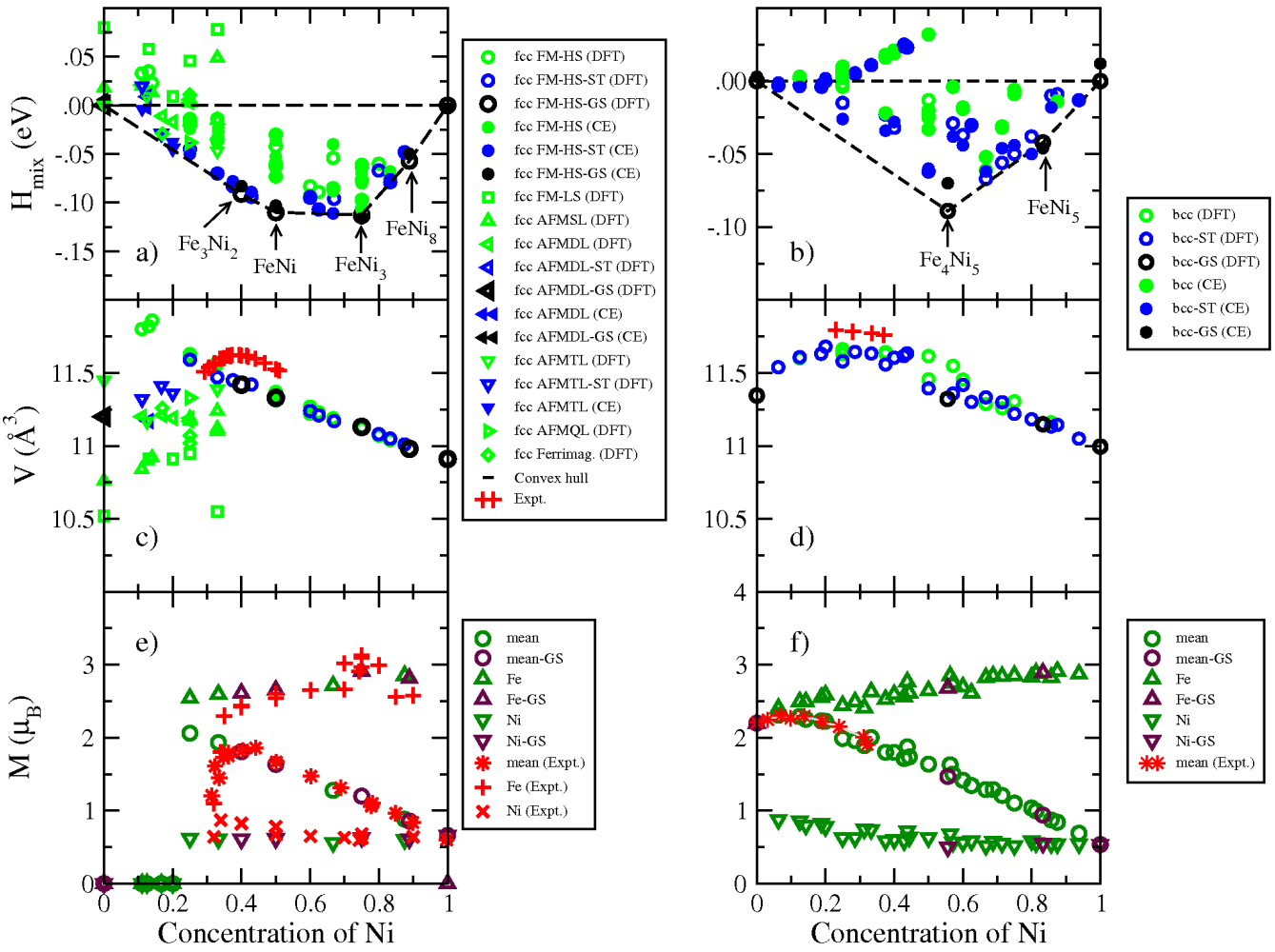

FIG. 1. (Color online) Enthalpies of mixing (a,b), volumes per atom (c,d) and magnetic moments (e,f) of Fe-Ni structures on fcc (a,c,e) and bcc (b,d,f) lattices, calculated using DFT. Experimental data are taken from Refs. 53, 56, and 57. GS refers to the ground state on fcc (a,c) or bcc (b,d) crystal lattices; ST is the most stable structure and magnetic configuration for the corresponding alloy composition.

0.023 eV/atom less stable, and has the atomic volume of 11.39 $\AA^3$, whereas AFMSL is 0.039 eV/atom less stable than FM and has the volume of 11.24 $\AA^3$ per atom. Coexistence of structures with different magnetic order and different atomic volumes but similar energies explains the Invar effect[69].

C. Fe-Cr binary alloys

The extensive theoretical[30–32,70–76] and experimental[77] investigations show that bcc Fe-Cr alloys at low Cr concentration form intermetallic phases with the most stable structures containing between 6.25 and 7.41 at. % Cr[30,76]. Our calculations shown in Fig. 2(b) confirm those findings for bcc Fe-Cr system. On fcc lattice, we predict three new ground states: $Fe_3Cr(L1_2)$, $FeCr_2(\beta 2(100)^{33})$, and $FeCr_8$ (Pt_8Ti-like) that are all significantly less stable than the bcc structures, see Figs. 2(a) and 5. Enthalpies of mixing of ordered Fe_3Cr and $FeCr_2$ structures are -0.111 and -0.120 eV/atom, respectively, and are approximately 0.05 eV/atom lower than those calculated for fcc Fe-Cr random alloys.

Comparison between enthalpies of mixing of fcc and bcc Fe-Cr alloys calculated using DFT and CE is shown in Figs. 2(a) and 2(b). A full set of ECIs derived by mapping DFT energies to CE is given in Fig. 4(c,d) and Table VIII in Appendix C. The cross-validation error between DFT and CE is 11.3 and 10.6 meV/atom for fcc and bcc Fe-Cr alloys, respectively. Similarly to fcc Fe-Ni alloys, the first and third nearest neighbour (1NN and 3NN) pair interactions are

positive and the second nearest neighbour (2NN) interaction is negative, favouring the $L1_2$ intermetallic phase, which is also the ground state of fcc Fe-Cr alloy. The 1NN pair interaction in bcc Fe-Cr alloys is negative, like in bcc Fe-Ni alloys, implying repulsive interaction between the unlike atoms in the first nearest neighbour coordination shell. ECIs of bcc Fe-Cr were previously analysed in Ref. 32. Despite the fact that our DFT calculations were performed using a different set of clusters, our results are in agreement with Ref. 32 in that the dominant negative 1NN pair interaction and positive fifth nearest neighbour pair interaction together give rise to the formation of Fe - 6.25 at.% Cr α-phase.

Atomic volumes of bcc Fe-Cr alloys in a broad range of alloy compositions are nearly constant, with some small variation in the range of 0.3 $\mathring{A}^3$ per atom, see Fig.2(d). There are two exceptions to this rule. Volume per atom of pure Cr and Cr-rich alloys decreases as a function of Fe content. This can be explained by the fact that Fe impurities influence anti-ferromagnetic order in pure Cr, reducing the magnitude of magnetic moments and the strength of magnetic interactions, see Fig. 2(f). This also affects the atomic volume. In Fe-rich alloys, atomic volume increases linearly with Cr content, reaching maximum of 11.50 $\mathring{A}^3$ per atom at 8.33 at. % Cr. The latter confirms previous theoretical predictions obtained using CPA and SQS methods[74,75] that show a local maximum of atomic volume (lattice parameter) of random bcc Fe-Cr alloys at approximately 10 at. % Cr. These theoretical predictions are in agreement with experimental data[78], where the observed deviation from Vegard's law is the largest at $\sim$ 10 at. % Cr . This phenomenon is probably caused by magneto-volume coupling and strong anti-ferromagnetic interaction between Fe and Cr atoms. At low density magnetic moments are larger and the energy of atomic structure is lower, hence Cr impurities in Fe tend to increase volume per atom in the α-phase. The increase is almost linear in Cr content until a critical concentration is reached and Cr starts segregating.

At variance with DFT analysis of ordered structures performed here, and studies of random alloys[74,75], the experimentally measured atomic volume in alloys with Cr concentration larger than 10 % continues to increase linearly towards the pure Cr limit. The discrepancy is caused by the fact that neither the ordered structures treated here nor the random alloys investigated in Refs. 74 and 75 are representative of real bcc Fe-Cr alloys, which are mixtures of α-phase and Cr clusters, as shown in Figs. 2(b,d) by black circles[32].

Composition dependence of atomic volume in fcc Fe-Cr alloys differs significantly from what is found in fcc Fe-Ni alloys. Due to strong anti-ferromagnetic interaction between Fe and Cr atoms, anti-ferromagnetic or ferri-magnetic order dominates in the entire range of alloy compositions, see Fig. 2(e). Volume decrease caused by anti-ferromagnetic ordering in Fe-rich fcc Fe-Ni alloys is also present in the entire range of alloy compositions. Volume decrease as a function of Cr concentration is particularly strongly pronounced in Cr-rich fcc Fe-Cr alloys.

Magnetic moments of Fe and Cr atoms as well as the average magnetic moment of ordered bcc Fe-Cr structures are similar to those predicted for random alloys in Refs. 29 and 74. They agree well with the available experimental data[79–81].

D. Cr-Ni binary system

Both DFT and CE simulations of fcc Cr-Ni alloys were performed in Ref. 59. Our analysis confirms the conclusion, derived from simulations and experiment, that there is only one globally stable ground state of the alloy, realized on the $CrNi_2$ ($MoPt_2$-like) ordered structure. We find further five fcc ground states: Cr_7Ni (of $Cmmm$ symmetry, predicted by CE), Cr_5Ni (also predicted by CE, with $Cmmm$ symmetry), Cr_3Ni-Z1(100), Cr_5Ni_2 (of $I4/mmm$ symmetry, also predicted by CE), and Cr_2Ni-β1(100). The latter is characterized by large positive enthalpy of formation and is less stable than bcc structures with the same composition, see Figs. 3(a) and 5. We find only one alloy configuration on bcc lattice that has small negative enthalpy of mixing, CrNi (predicted by CE, with $Cmmn$ symmetry and $H_{mix} = -4$ meV/atom).

Comparison between enthalpies of mixing of fcc and bcc Cr-Ni alloys calculated using DFT and CE is given in Fig. 3(a,b). A full set of ECIs found by mapping the energies of structures from DFT to CE are given in Fig. 4 and Table VIII in Appendix C. Cross-validation errors between DFT and CE are 14.2 and 12.8 meV/atom for fcc and bcc Cr-Ni alloys, respectively. Similarly to fcc Fe-Ni and Fe-Cr alloys, the first and third nearest neighbour (1NN and 3NN) pair interactions in fcc Cr-Ni alloys are positive and the second nearest neighbour (2NN) interaction is negative. Unlike the other two binary systems, the ground state of fcc Cr-Ni alloys is $MoPt_2$-like phase. The ECI parameters derived from our DFT calculations and the cross-validation error between DFT and CE are in agreement with those of Ref. 59. The negative 1NN pair interaction in bcc Cr-Ni system is the strongest of all the binary alloys. Because of that, there is only one bcc intermetallic phase, CrNi, of $Cmmn$ symmetry, which has small negative enthalpy of mixing (-4 meV/atom).

Variation of atomic volume as a function of Ni content in both fcc and bcc structures is more linear than in Fe-Ni and Fe-Cr alloys because magnetic interactions are weaker, see Figs. 3(c-f). Similarly to Fe-Cr alloys, the difference between atomic volumes of alloys with low and high concentration of Cr is more significant for fcc than bcc lattice.

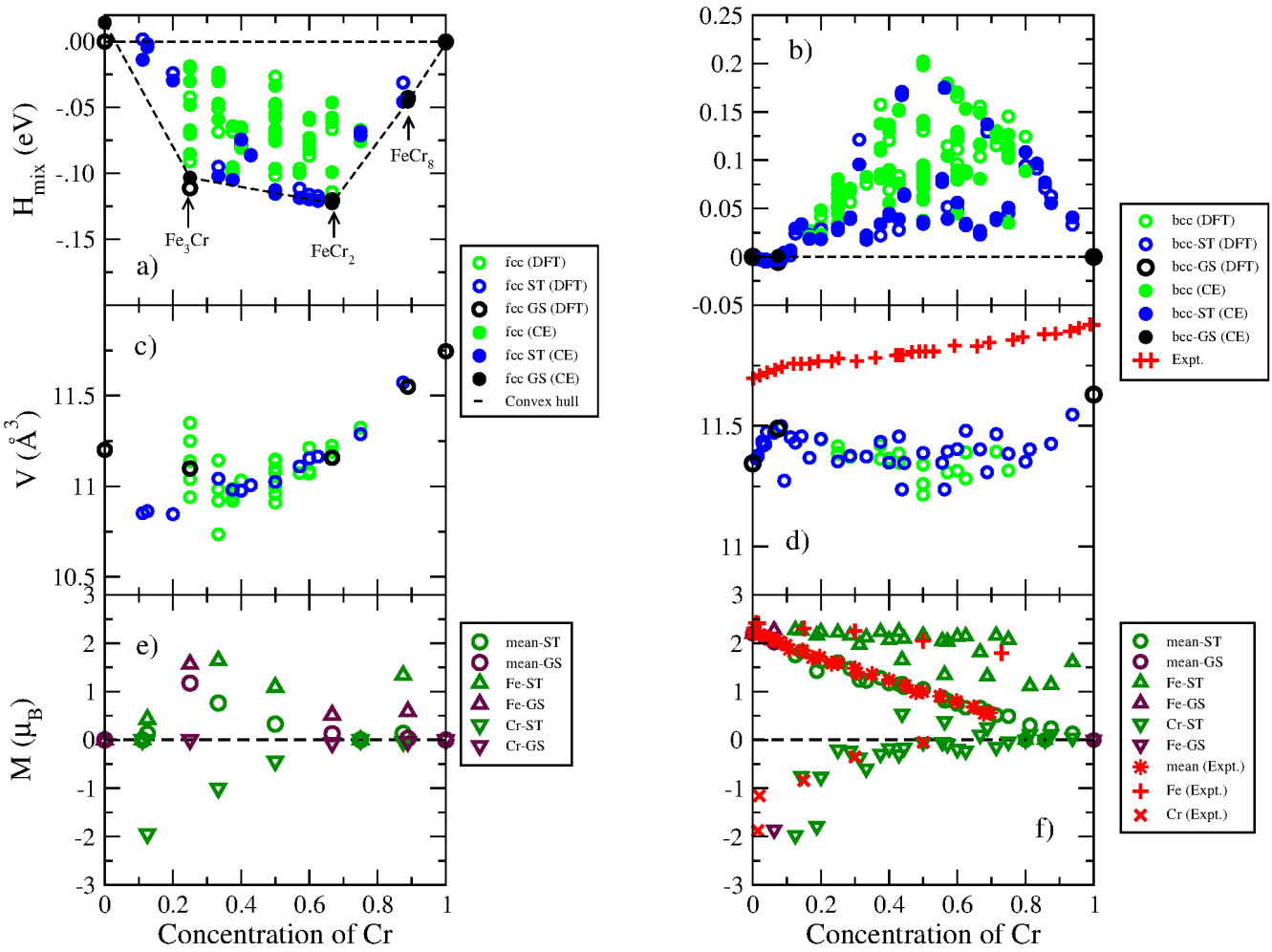

FIG. 2. (Color online) Enthalpies of mixing (a,b), volumes per atom (c,d) and magnetic moments (e,f) calculated using DFT for Fe-Cr alloys on fcc (a,c,e) and bcc (b,d,f) lattices, respectively. Experimental data are taken from Refs. 79–81. GS - ground states of alloys on fcc (a,c) or bcc (b,d) crystal lattices, respectively; ST - the most stable structure at a given composition.

E. Fe-Cr-Ni ternary system

The stability of fcc and bcc phases of ternary Fe-Cr-Ni alloys, and the corresponding binary alloys, is defined with respect to bcc Fe, bcc Cr and fcc Ni, as mentioned previously. Enthalpies of formation of Fe-Ni, Fe-Cr and Cr-Ni alloys are shown in Figs. 5(a), 5(b) and 5(c), respectively. The Ni-rich fcc Fe-Ni and Cr-Ni alloys are usually more stable than bcc alloys of similar composition, whereas alloys with smaller Ni content tend to adopt bcc structure. In Fe-Cr alloys, energies of fcc phases are always higher than the energies of bcc structures. Still, meta-stable fcc Fe-Cr structures and interactions between the unlike atoms in fcc Fe-Cr alloys proves critical to understanding chemical ordering in Fe-Cr-Ni alloy system. From the list of ground states associated with each lattice type shown in Figs. 1, 2 and 3, we conclude that there are only four binary fcc phases: FeNi, $FeNi_3$, $FeNi_8$ and $CrNi_2$, and only one binary bcc Fe-Cr phase, namely the α-phase, which are the global ground states of the alloys. Enthalpies of formation, volumes and magnetic moments per atom, and space groups of the relevant alloy structures are given in Table III.

Enthalpies of formation of fcc and bcc Fe-Cr-Ni alloys derived from DFT and CE are compared in Fig. 6. The most stable fcc and bcc structures form convex hulls, shown in Fig. 6 by blue and red surfaces, respectively. The line of intersection between these two surfaces corresponds to the zero Kelvin fcc-bcc phase transition, which occurs as a function of alloy composition. There is no Fe-Cr-Ni ternary alloy configuration on bcc lattice that has negative enthalpy of formation. Fcc alloy structures have negative enthalpy of formation in the Ni-rich limit of alloy compositions. This region of negative enthalpy of formation is elongated along the Fe-Ni edge of the alloy composition triangle. The $L1_2$-based fcc Fe_2CrNi phase, similar to Cu_2NiZn alloy phase, is the global ground state of Fe-Cr-Ni alloys. The

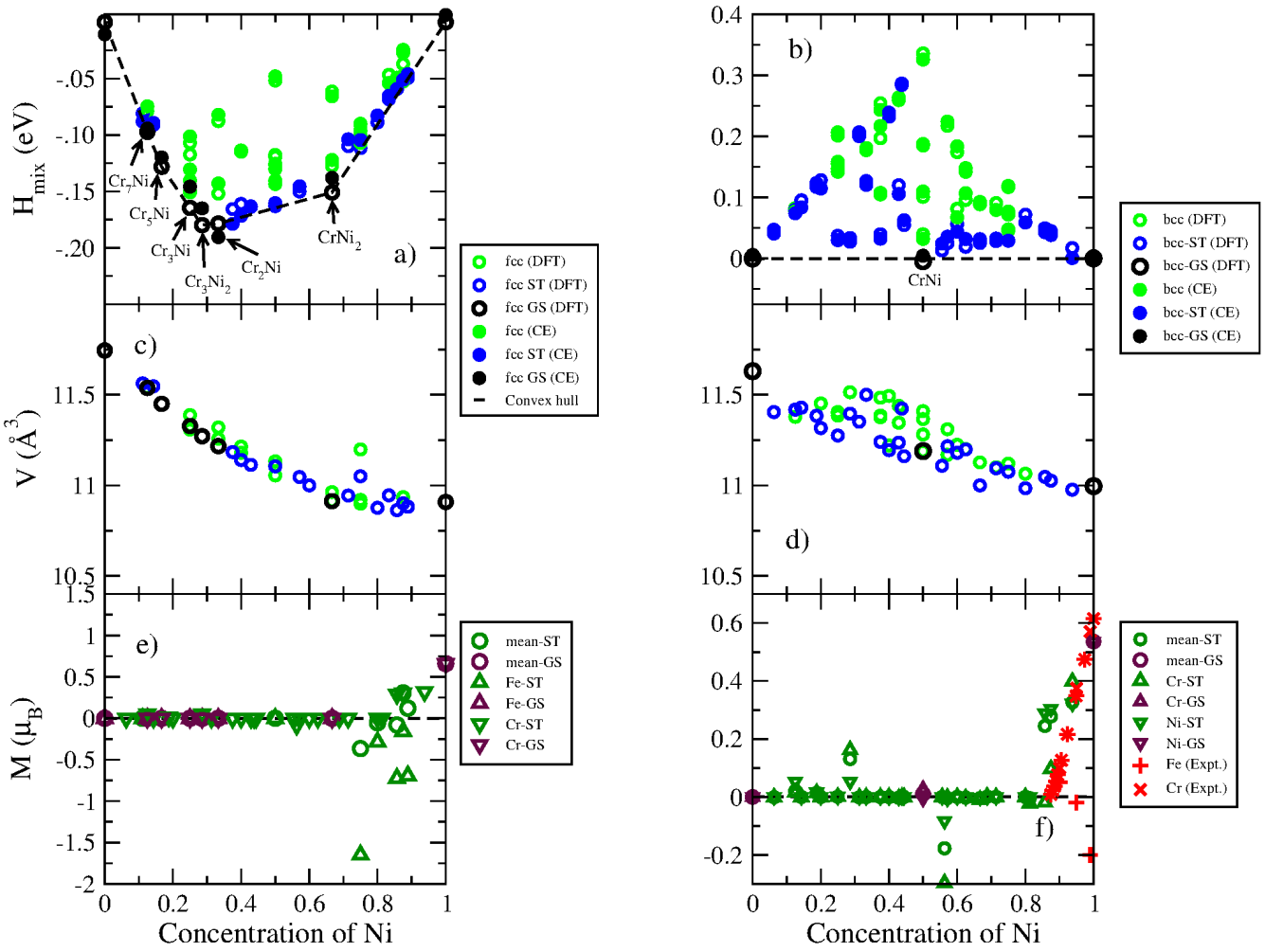

FIG. 3. (Color online) Enthalpies of mixing (a,b), volumes per atom (c,d) and magnetic moments (e,f) calculated using DFT for Cr-Ni alloys on fcc (a,c,e) and bcc (b,d,f) lattices, respectively. Experimental data are taken from Ref. 56. GS - ground states of alloys on fcc (a,c) or bcc (b,d) lattices, respectively; ST - the most stable structure found for a given alloy composition.

enthalpy of formation, volume per atom, magnetic moments of each atom, as well as the space group of Fe_2CrNi structure, are given in Table III.

ECIs of ternary fcc and bcc alloys are derived by mapping DFT energies onto CE for 248 fcc and 246 bcc structures, respectively. In CE simulations we used the same set of clusters as in fcc (five two-body, three three-body, two four-body, one five-body clusters) and bcc (five two-body, two three-body, one four-body, one five-body clusters) binary alloys. Since in ternary alloys each cluster can be decorated by point functions in different ways (see Section II.A and Table I), the number of ECIs is much larger than the number of clusters taken into consideration. Namely, we have 15 two-body, 16 three-body, 14 four-body, 12 five-body clusters for fcc alloys and 15 two-body, 12 three-body, 6 four-body, 18 five-body clusters for bcc alloys. Values of all the optimized ECIs for ternary alloys are given in Fig. 7 and Table I. Cross-validation errors between DFT and CE are 10.2 and 11.2 meV/atom for fcc and bcc ternary alloys, respectively.

Volumes per atom of fcc and bcc Fe-Cr-Ni ternary alloy structures computed using DFT at 0K are shown in Fig. 8. Both fcc and bcc alloy configurations exhibit the largest volume per atom in the Cr-rich corner of the diagram. Atomic volume is the smallest in the Ni-rich corner. Difference between the two values is larger for fcc alloys. Atomic volumes of fcc structures exhibit a significant degree of non-linearity as functions of alloy composition. This is explained by the different magnetic behaviour of fcc and bcc alloys, see Figure 9(a-d), treated as a functions of composition. A relation between fcc-bcc phase stability and magnetic moments of the most stable structures, as well as the discontinuity in the magnitude of the average magnetic moment at the fcc-bcc phase transition line, are illustrated in Fig. 9(e).

Average magnetic moments of bcc alloys are linear functions of Fe content. Magnetic moments are maximum for the

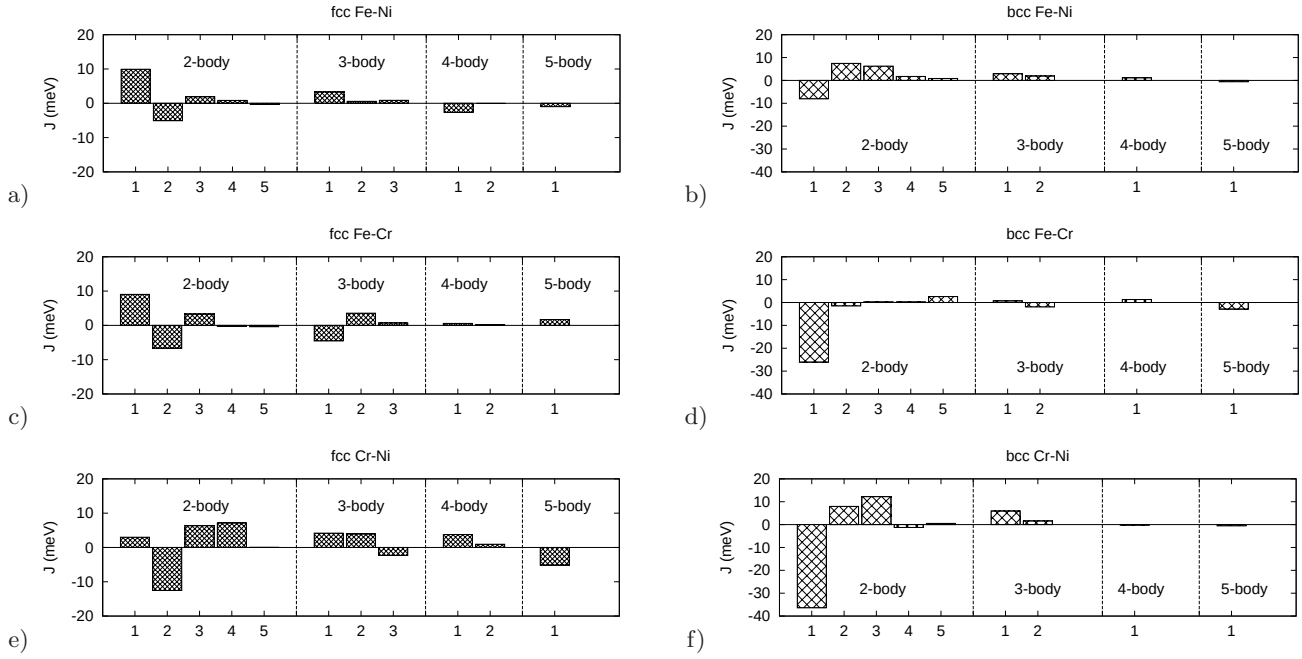

FIG. 4. Effective cluster interactions (ECIs) derived using CE method for fcc Fe-Ni (a), bcc Fe-Ni (b), fcc Fe-Cr (c), bcc Fe-Cr (d),fcc Cr-Ni (e), bcc Cr-Ni (f) alloys.

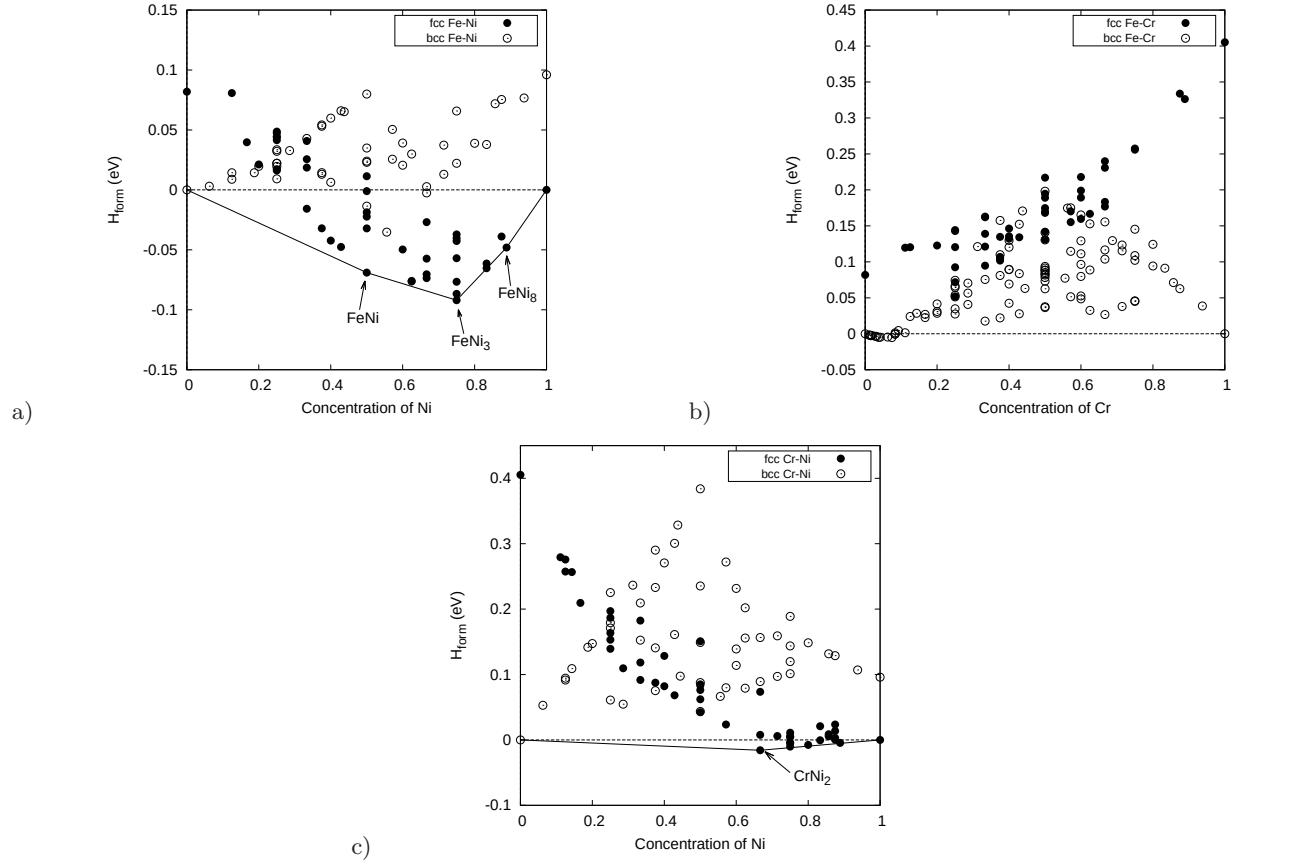

FIG. 5. Enthalpies of formation of Fe-Ni (a), Fe-Cr (b), and Cr-Ni (c) binary structures.

TABLE III. Enthalpies of formation of the lowest energy intermetallic phases of fcc Fe-Cr-Ni ternary alloys.

Structure	Space group	Wyckoff positions	Mag. space group	(Mag.) Wyckoff positions	V (eV)	H_{form} H_{form}	M (μ_B)
FeNi	$P4/mmm$	Fe_1 2e	$P4/mm'm'$	Fe_1 2e	11.33	-0.069	2.66
($L1_0$)		Ni_1 1a		Ni_1 1a			0.63
		Ni_2 1c		Ni_2 1c			0.63
$FeNi_3$	$Pm-3m$	Fe_1 1a	$Pm'm'm$	Fe_1 1a	11.13	-0.091	2.91
($L1_2$)		Ni_1 3c		Ni_1 1f			0.59
				Ni_2 1d			0.58
				Ni_3 1g			0.72
$FeNi_8$	$I4/mmm$	Fe_1 2a	$P-1$	Fe_1 1a	10.98	-0.051	2.81
($NbNi_8$)		Ni_1 8h		$Ni_1$2i			0.60
		Ni_2 8i		Ni_2 2i			0.63
				Ni_3 2i			0.61
				Ni_4 2i			0.61
$CrNi_2$	$Immm$	Cr_1 2a	$Immm1'$	Cr_1 2a	10.91	-0.016	0.00
($MoPt_2$)		Ni_1 4e		Ni_1 4e			0.00
Fe_2CrNi	$P4/mmm$	Cr_1 1c	$Pm'm'm$	Cr_1 1f	11.37	-0.026	-2.44
(Cu_2NiZn)		Fe_1 2e		Fe_1 1d			2.05
		Ni_1 1a		Fe_2 1g			2.12
				Ni_1 1a			0.15

Fe-rich alloy compositions and minimum for anti-ferromagnetic Cr-rich alloys. Fcc Fe-rich structures do not develop large average magnetic moments because ferromagnetic order ib fcc alloys is replaced with anti-ferromagnetic order, like in Fe-Ni alloys (see Section III.B). Furthermore, Cr-rich alloy structures have relatively small magnetic moments. Structures near the centre of the composition triangle, characterized by the approximately equal amounts of Fe, Cr and Ni, have relatively small average magnetic moments. The average magnetic moment decreases rapidly with increasing Cr content. For example, the average atomic magnetic moment in fcc $(Fe_{0.5}Ni_{0.5})_{1-x}Cr_x$ alloys is 1.63, 0.97, 0.69 and 0.00 μ_B for Cr content $x = 0.0$, 0.2, 0.33 and 0.5, respectively. These results are in agreement with experimental observations, performed at 4.2K, and showing that magnetization decreases rapidly in $Fe_{0.65}(Cr_xNi_{1-x})_{0.35}$ alloys as a function of Cr content in the interval from $x = 0.0$ to 0.2[82]. This effect is also responsible for the observed reduction of the Curie temperature as a function of Cr content in $Fe_{0.65}(Cr_xNi_{1-x})_{0.35}$ and $(Fe_{0.5}Ni_{0.5})_{1-x}Cr_x$ alloys, described in Refs. 82 and 83. Non-linear variation of magnetic moments as functions of alloy composition results in deviations from Vegard's law in fcc alloys. Despite the fact that Cr atoms have larger size, volume per atom of fcc $(FeNi)_{1-x}Cr_x$ alloys decreases as a function of x, and is 11.33, 11.20, 11.09 and 10.92 $\mathring{A}^3$/atom for $x = 0.0$, 0.2, 0.33 and 0.5, respectively. Results for other compositions are given in Supplementary Material Part 2.

Magnetic moments of each component of fcc and bcc alloys are shown in Fig. 10. The results show a rapid decrease of magnetic moments on Ni sites as functions of Cr content in fcc alloys (where magnetic moments on Ni sites in alloys containing more than 33% Cr are close to zero). Cr atoms prefer having their magnetic moments ordered anti-ferromagnetically with respect to the Fe and Ni moments. Their magnitudes are larger at low Cr concentration, however even at 25 % Cr content they are still fairly large (-2.44 μ_B and -2.53 μ_B for Fe_2CrNi and $FeCrNi_2$ structures). Because of strong anti-ferromagnetic interactions between Fe and Cr atoms, structures with large magnetic moments on Cr sites also have large magnetic moments on Fe sites (2.09 μ_B and 2.31 μ_B for Fe_2CrNi and $FeCrNi_2$ structures). An exception from this rule is the Fe-rich corner of the diagram, where fcc structures remain anti-ferromagnetic and the mean magnetic moment as well as average magnetic moments of the constituting components are equal or close to zero.

Similarly to fcc structures, magnetic moments of Cr atoms on bcc lattice in the dilute Cr limit order anti-ferromagnetically with respect to those of Fe and Ni atoms, and their magnitudes decrease rapidly as a function of Cr concentration. For example, magnetic moments of Cr atoms in bcc Fe_2CrNi and $FeCrNi_2$ structures are -0.19 μ_B and -0.12 μ_B. In other words, they are an order of magnitude smaller than those found in fcc alloy structures. Furthermore, Cr-rich structures are not non-magnetic, like they are in the fcc case, but anti-ferromagnetic. Unlike Cr atoms, the magnitudes of magnetic moments on Fe and Ni sites are larger in bcc than in fcc structures. Average magnitudes of moments on Fe sites are larger than 1 μ_B for most of the compositions, with the maximum value of 2.94

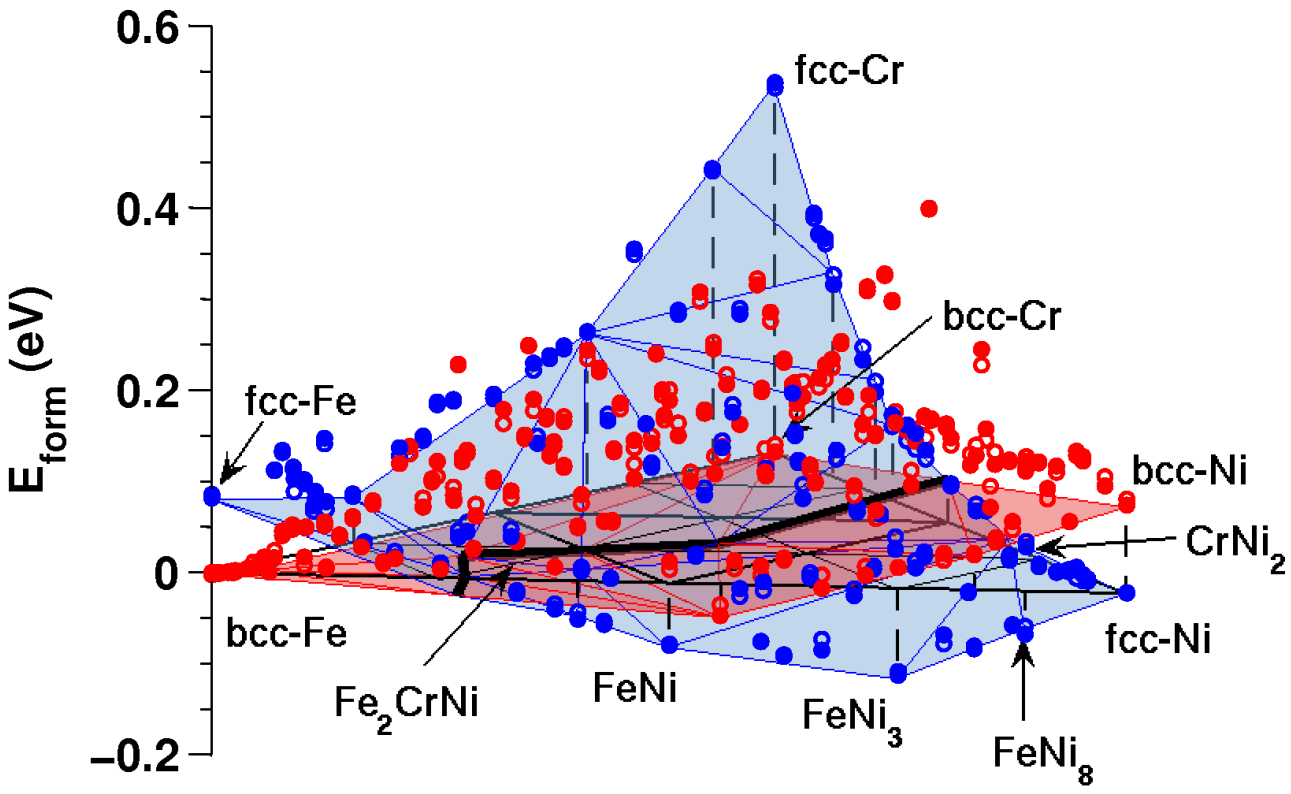

FIG. 6. (Color online) Enthalpies of formation predicted by DFT (filled circles) and CE (open circles) calculations for ternary Fe-Cr-Ni alloys at 0K. Only the most stable structures for each composition are shown. Blue and red circles show values calculated for fcc and bcc Fe-Cr-Ni ternary alloys, whereas blue and red surfaces show convex hulls for fcc and bcc crystal structures, respectively. Black solid line corresponds to the line of intersection between fcc and bcc convex hulls. Cross-validation errors between DFT and CE are 10.2 and 11.2 meV/atom for fcc and bcc ternary alloys, respectively.

μ_B corresponding to $FeCrNi_{14}$ structure in the Ni-rich corner of the diagram. Average magnetic moments of Ni atoms are close to 0 μ_B only in bcc Cr-rich Cr-Ni binary alloys. As the Fe content increases, the average magnetic moment of Ni atoms increases, too, reaching the maximum value of 0.86 μ_B in the Fe-rich corner, modelled by $Fe_{14}CrNi$ structure.

IV. FINITE TEMPERATURE PHASE STABILITY OF FE-CR-NI ALLOYS

A. Enthalpy of formation

The finite temperature phase stability of Fe-Cr-Ni alloys was analyzed using quasi-canonical MC simulations and ECIs derived from DFT calculations. MC simulations were performed for 63 different compositions spanning all the binary and ternary Fe-Cr-Ni alloys on a 10% composition mesh for each of the three constituents of the alloy, and additional 12 compositions with Cr and Ni content varying from 5% to 35% and from 25% to 45%, respectively, to increase the composition mesh density in the vicinity of the fcc-bcc phase transition line.

Enthalpies of formation of fcc and bcc alloys corresponding to 300 K, 600 K and 900 K are shown in Fig. 11. At 300 K, in fcc and bcc alloys there is a large region of concentrations where enthalpies of mixing are negative, indicated in Fig. 11 by a blue colour. The origin of this phenomenon is related to the fact that alloys are decomposed into mixtures of pure elements and intermetallic phases. The negative formation enthalpies of fcc Fe-Cr-Ni alloys are driven mainly by the existence of fcc FeNi, $FeNi_3$, $FeNi_8$ and $CrNi_2$ binary phases and fcc Fe_2CrNi ternary phase. In the case of bcc Fe-Cr-Ni alloys this phenomenon is associated primarily with Fe-Cr α-phase and Fe_4Ni_5 VZn-like phase that is the

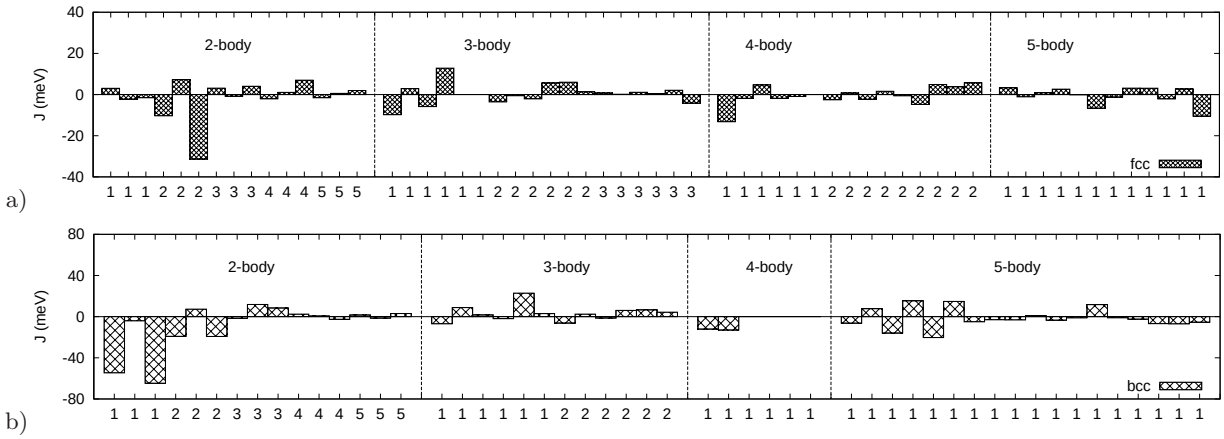

FIG. 7. Effective cluster interactions obtained using CE method for fcc (a) and bcc (b) Fe-Cr-Ni ternary alloys.

most stable Fe-Ni phase on bcc lattice. The latter one has not been experimentally observed since it is significantly less stable than the corresponding fcc phases. At 600K and 900K, the regions of negative enthalpy of formation become smaller, however their shrinkage is more significant between 600K and 900K than at lower temperatures. This is related to the fact that most of the intermetallic phases in Fe-Cr-Ni system are ordered at 600K and disordered at 900K, see Table V. This point is discussed in the next subsection in greater detail.

Comparing the formation enthalpies of fcc and bcc alloys, we can identify the fcc-bcc phase transition line as a function of alloy composition, see Fig. 11. Since in our model vibrational and magnetic contributions at elevated temperatures are not taken into account, the enthalpies of formation derived from MC simulations and shown in Fig. 11 refer to 0K DFT energies of pure Fe, Cr and Ni. While this approximation is valid at relatively low temperatures, at high temperatures it breaks down. For example, pure iron at low temperatures is stable in bcc α-phase, see Table II, whereas at 1185 K[84] it transforms into the fcc γ-phase, and then back into the bcc δ-phase. In order to investigate the formation enthalpies of alloys at high temperature one should at least take into account the effect of thermal magnetic excitations in Fe. The following correction can then be applied to the formation enthalpies in the high temperature limit. It is proportional to the concentration of Fe and is based on results given in Fig. 2 of Ref. 72:

$$\Delta H_{lat}^{corr} \approx c_{Fe}\left[(E_{lat}(T) - E_{lat}(0)) - (E_{GS}(T) - E_{bcc}(0))\right], \tag{22}$$

where $lat = fcc, bcc$, $E_{lat}(0)$ and $E_{lat}(T)$ are the energies of Fe on lat at 0K and at temperature T, $E_{bcc}(0)$ is the energy of bcc ground state of Fe and $E_{GS}(T)$ is the temperature-dependent energy of the ground state, which is *either* fcc *or* bcc.

The enthalpies of formation computed in this way for $T = 1600$K, are compared to experimental data from Refs. 85 and 86 in Fig. 12. Without the above magnetic correction, the predicted region of negative enthalpies of formation is significantly smaller in comparison with experimental data. However, if the magnetic correction is implemented, predictions agree with experiment very well. The theoretical line dividing the regions with positive and negative enthalpies of formation matches the experimental line shown in Fig. 12(c) (see also Supplementary Material Part 2 for details). The magnetic contribution to the enthalpy of formation is also important for predicting the position of the fcc-bcc phase transition line. As shown in Figs. 12(a) and 12(b), the Ni-rich region of stable fcc alloys predicted with this correction applied, is significantly larger and is in much better agreement with the available experimental findings and CALPHAD simulations (see e.g. Fig. 7(a) in Ref. 87 with results at 1573 K).

Phase stability treated as function of temperature was examined by using MC simulations more extensively for one particular composition, $Fe_{70}Cr_{20}Ni_{10}$, which can be used to investigate properties of austenitic 304 and 316 steels[20]. As shown in Fig. 11, at 300K, 600K and 900K the $Fe_{70}Cr_{20}Ni_{10}$ alloy belongs to the Fe-rich region of stability of bcc alloys, in agreement with experimental data and CALPHAD simulations (see e.g. Fig. 6 of Ref. 14 referring to 500 °C). At 1600K, with the above magnetic correction applied, fcc alloy is more stable than bcc alloy, and its calculated enthalpy of formation of 0.030 eV/atom, obtained from MC simulations at 1600K, is close to the experimental value of 0.035 eV/atom measured at 1565 K[85].

Since the austenitic stainless steels are formed by rapid cooling from approximately 1323K, we also analyse the phase stability of $Fe_{70}Cr_{20}Ni_{10}$ alloy at 1300K[8,36]. Similarly to the 1600K case, with the magnetic correction applied, fcc alloys have lower formation enthalpy than bcc alloys. The stability of various magnetic configurations of $Fe_{70}Cr_{20}Ni_{10}$ was analyzed using spin-polarized DFT calculations for the fcc structure with 256 atoms, derived from MC simulations at 1300K. As shown in Table IV, the AFMSL and FM configurations are more stable than the AFMDL configuration,

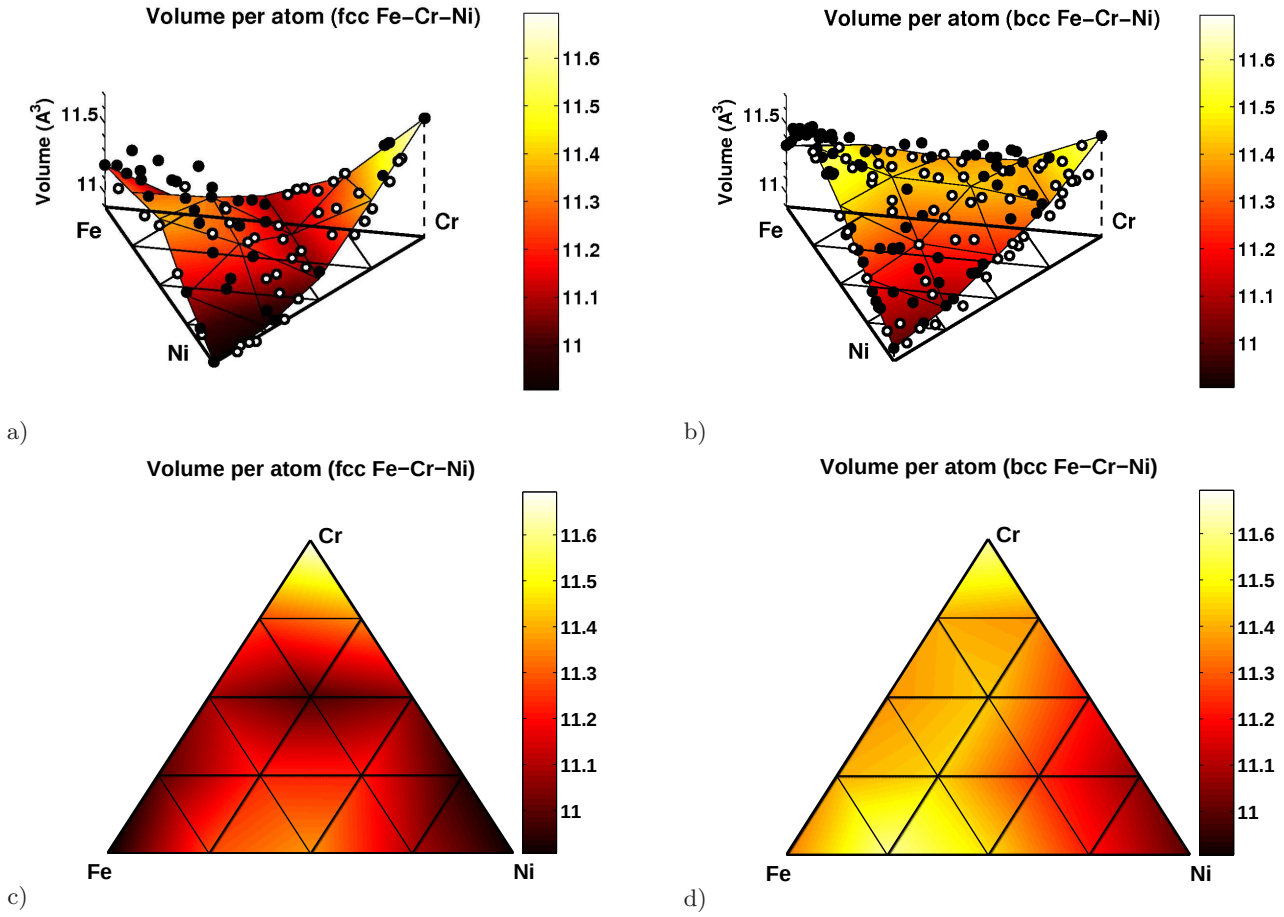

FIG. 8. (Color online) Volumes of stable fcc (a, c) and bcc (b, d) ordered structures predicted by DFT calculations at 0K for various alloy compositions. Filled and open circles in (a, b) correspond to DFT data above and below the interpolated values, represented by the respective surfaces. (c, d) are the orthogonal projections of (a, b).

and the formation enthalpies of the two former ones are 0.018 eV/atom and 0.015 eV/atom higher than the value obtained from equilibrium MC simulations at 1300K. Results for the MC-generated structure are compared in Table IV also with enthalpies of formation of various magnetic configurations performed using fcc SQS with 256 atoms given in Ref. 20. The energy of the most stable AFMSL configuration on SQS is 0.049 eV/atom higher than the energy of the most stable FM configuration realized on the MC-generated structure, and 0.064 eV/atom higher than the energy evaluated using equilibrium MC simulations at 1300K. Since the MC model with magnetic correction was successfully validated against experimentally observed enthalpies of formation, as described above, one can conclude that SQS-based calculations lead to the overestimation of formation enthalpy for the considered alloy composition. Hence, even at high temperatures, the configurations generated using CE combined with MC simulations describe $Fe_{70}Cr_{20}Ni_{10}$ alloy better than SQS.

B. Order-disorder transitions

There is experimental evidence confirming the presence of chemical order in Fe-Cr-Ni alloys. Bcc alloys at low temperatures segregate, with intermetallic Fe-Cr α-phase representing the only known exception, whereas fcc alloys form austenitic steels exhibiting the formation of chemically ordered phases[22–25].

Ordering temperatures correspond to inflection points on the energy-temperature curves. Below these temperatures, chemically ordered phases are formed. For example, Fe_2CrNi intermetallic phase remains ordered below 650K, whereas order between Fe and Cr, and Cr and Ni pairs of atoms in fcc $Fe_{50}Cr_{25}Ni_{25}$ alloy vanishes above 1450 K, see Fig. 14. Ordering temperatures computed for all the fcc ground states of Fe-Cr-Ni alloys are given in Table V. Fcc Fe_3Cr $L1_2$ phase has the highest ordering temperature of 1550K. This phase is however less stable than the bcc phase with the

TABLE IV. Enthalpies of formation of $Fe_{70}Cr_{20}Ni_{10}$ alloy derived from MC simulations at 1300K and 1600K, compared with experimental values measured at 1565 K[85], and with DFT energies computed for SQS and MC-generated atomic structures.

	without corr.	with corr.	Expt.
MC at 1600 K			
bcc	0.028	0.045	
fcc	0.087	0.030	0.035
MC at 1300 K			
bcc	0.017	0.029	
fcc	0.051	-0.006	
DFT (SQS)[a]			
fcc AFMSL	0.115		
fcc AFMDL	0.126		
fcc FM	0.116		
DFT (MC structure)[b]			
fcc AFMSL	0.069		
fcc AFMDL	0.105		
fcc FM	0.066		

[a] SQS structure from Ref. 20.
[b] Structure generated using MC simulations performed at 1300 K.

same composition. Ordering temperatures predicted for FeNi, $FeNi_3$ and $CrNi_2$ alloys are in reasonable agreement with experimental data. The highest order-disorder transition temperatures $T_{ord-disord}$, corresponding to inflection points of energy-temperature curves, above which alloys can be described as disordered, were found using Monte Carlo simulations for the entire range of alloy compositions, and are shown in Fig. 13. Values of $T_{ord-disord}$ for fcc Fe-Cr-Ni alloys, see Fig. 13(a) vary non-linearly as functions of composition, exhibiting even some local maxima. A local maximum near $FeNi_3$ phase is in fact expected since $FeNi_3$ forms $L1_2$ phase with relatively high ordering temperature. A local maximum around another experimentally known binary phase, $CrNi_2$ ($MoPt_2$), can also be recognized in Fig. 13, however it is not as pronounced as in the $FeNi_3$ case. Two others maxima are less strongly pronounced. The first one corresponds to fcc alloys with Cr content between 25% and 50% and is not very important for applications since fcc alloys in this composition range are less stable than bcc alloys. More significant is the large region of Cr content from 10% to 50% and Ni content from 0% to 50%, which partially overlaps with the range of stability of austenitic steels. Many Fe-Cr-Ni chemically ordered alloys are inside this region, with examples including $Fe_{64}Cr_{16}Ni_{20}$ and $Fe_{59}Cr_{16}Ni_{25}$[22], $Fe_{56}Cr_{21}Ni_{23}$[23], and $Fe_{66.2}Cr_{17.5}Ni_{14.5}Mo_{2.8}$[88].

All the bcc Fe-Cr-Ni alloys have high order-disorder temperatures, see Fig. 13(b). Hence they are characterized by short range order even at temperatures close to the experimental melting point. The predicted very high order-disorder temperatures may be overestimated due to the fact that our DFT-based Monte Carlo simulations neglect vibrational and magnetic contributions[89,90].

Analysis of variation of predicted $T_{ord-disord}$ as functions of alloy composition confirms the experimentally observed reduction of atomic ordering in $(FeNi_3)_{1-x}Cr_x$ alloys annealed at 486 °C (=759K) as a function of Cr content in the composition interval from x=0.0 to 0.17[25]. The values of $T_{ord-disord}$ obtained from MC simulations for $FeNi_3$ and $(FeNi_3)_{0.8}Cr_{0.2}$ alloys are 950K and 750K, respectively. Alloys with lower Cr content have order-disorder transition temperature significantly higher than the annealing temperature used in the above experiments[25]. Values of $T_{ord-disord}$ in alloys with high Cr content are lower than the above annealing temperature.

C. Short-range order parameters

Chemical order in alloys is characterized by the Warren-Cowley short-range order parameters, α_1^{i-j} and α_2^{i-j}, for the first (1NN) and second (2NN) nearest neighbour coordination shells. These parameters are calculated from Eq. 21 using correlation functions deduced from MC simulations. MC simulations were performed for various temperatures for binary alloys and four ternary compositions: $Fe_{56}Cr_{21}Ni_{23}$, $Fe_{42.5}Cr_{7.5}Ni_{50}$, $Fe_{38}Cr_{14}Ni_{48}$ and $Fe_{34}Cr_{20}Ni_{46}$, for which experimental SRO parameters were published in Refs. 23 and 24. SRO parameters obtained for binary alloys agree with experimental data, see Table VI. Comparison with experimental values for ternary Fe-Cr-Ni alloys is given

TABLE V. Enthalpies of mixing and ordering temperatures of several important intermetallic phases of Fe-Cr-Ni alloys.

Structure	ΔH_{mix} (eV)	T_{ord} (K)	$T_{ord}^{Expt.}$ (K)
fcc FeNi	-0.103	650	620[65]
fcc $FeNi_3$	-0.116	950	790[65]
fcc $FeNi_8$	-0.053	550	
fcc Fe_3Ni_2	-0.082	550	
fcc $CrNi_2$	-0.155	750	863[65]
fcc Cr_2Ni	-0.182	1250	
fcc Cr_3Ni	-0.153	1150	
fcc Fe_3Cr	-0.103	1550	
fcc $FeCr_2$	-0.119	850	
fcc $FeCr_8$	-0.052	350	
fcc Fe_2CrNi	-0.164	650	

in Fig. 15 and in Table VII. MC simulations performed for fcc $Fe_{56}Cr_{21}Ni_{23}$ alloy[23] show that it is characterized by pronounced Cr-Ni ordering, whereas at the same time there is no Fe-Ni ordering. Values of α_1^{Fe-Ni} and α_1^{Cr-Ni} are in excellent agreement with experimental observations. The calculated SRO parameter for Fe and Cr atoms is negative, in agreement with experimental observations, although the magnitude of this parameter predicted by calculations is larger. This again may be due to the fact that vibrational and magnetic contributions were neglected[89]. The effect of lattice vibrations on ordering in bcc Fe-Cr system was noted in Refs. 32, 72, and 90.

The effect of Cr on SRO in Fe-Cr-Ni alloys was analyzed, using MC simulations, for three compositions $Fe_{42.5}Cr_{7.5}Ni_{50}$, $Fe_{38}Cr_{14}Ni_{48}$ and $Fe_{34}Cr_{20}Ni_{46}$, which are the compositions investigated experimentally in Ref. 24. As expected, the absolute values of SRO parameters increase with decreasing temperature for both 1NN and 2NN (see Table VII). All the 2NN SRO parameters are positive for these three alloys. α_1^{Fe-Ni} and α_1^{Fe-Cr} are negative and their absolute values decrease as functions of Cr content. An interesting result is that the sign of α_1^{Cr-Ni} changes from positive for $Fe_{42.5}Cr_{7.5}Ni_{50}$ to negative for $Fe_{34}Cr_{20}Ni_{46}$ alloy. $Fe_{38}Cr_{14}Ni_{48}$ alloy with intermediate Cr content has positive $\alpha_1^{(Fe-Cr)}$ only at the relatively low temperature of 600K. Our theoretical results were compared with the measured SRO between Ni atoms and 'average' (Fe,Cr) atoms in $Fe_{42.5}Cr_{7.5}Ni_{50}$, $Fe_{38}Cr_{14}Ni_{48}$ and $Fe_{34}Cr_{20}Ni_{46}$ alloys, quenched rapidly from 1323K, annealed at 873K and irradiated at 583K with 2.5 MeV electrons[24]. The authors of Ref. 24 neglected ordering between Fe and Cr atoms, arguing that there was no evidence for the occurrence of stable Fe-Cr compounds at low temperatures. Their assumption was based also on experimental observations by Cenedese et al.[23] who found that in fcc $Fe_{56}Cr_{21}Ni_{23}$ alloy only Cr and Ni atoms were ordered.

To compare results of MC simulations with experimentally measured24 SRO parameters involving Ni and 'average' (Fe,Cr) atoms, effectively treating ternary Fe-Cr-Ni alloys as a pseudo-binary alloy of composition $Ni_x(FeCr)_{1-x}$, we defined an effective SRO parameter involving Ni and (Fe,Cr) atoms as

$$\alpha_n^{(Fe,Cr)-Ni} = \frac{c_{Fe}}{c_{Fe}+c_{Cr}}\alpha_n^{Fe-Ni} + \frac{c_{Cr}}{c_{Fe}+c_{Cr}}\alpha_n^{Cr-Ni}. \quad (23)$$

Values of $\alpha_1^{(Fe,Cr)-Ni}$ defined in this way and calculated using MC simulations at 1300K are in excellent agreement with experimental observations for an alloy sample quenched rapidly from 1323K. Despite the fact that experimental measurements for samples irradiated at 583K cannot be directly compared with MC simulations at 600K, experimental observations of the more pronounced chemical order in $Fe_{34}Cr_{20}Ni_{46}$ sample irradiated at 583K in comparison with $Fe_{38}Cr_{14}Ni_{48}$ sample are in agreement with our predictions.

Atomic ordering in Fe-Cr-Ni alloys can be explained by analysing interactions between pairs of Fe-Cr, Fe-Ni and Cr-Ni atoms, V_n^{ij}. They were derived from the two-body effective cluster interaction parameters for fcc and bcc Fe-Cr-Ni alloys listed in Table I. Assuming that many-body interactions are small, we find that V_n^{ij} are related to $J_{2,n}^{(s)}$ and can be calculated using Eq. 18. V_n^{Fe-Ni}, V_n^{Fe-Cr} and V_n^{Cr-Ni} computed for fcc and bcc ternary alloys are compared with values derived for binary alloys in Fig. 16. All the 1NN chemical pairwise interactions in bcc ternary alloys are even more negative than those found in binary alloys. This means that repulsion between Fe-Cr, Fe-Ni and Cr-Ni atoms in ternary alloys is even stronger than in binary alloy systems. On the other hand, in ternary fcc alloys the 1NN chemical pairwise interaction between Fe and Ni atoms vanishes almost completely. This results in that SRO involving Fe and Ni atoms in the first nearest neighbour coordination shell measured in Ref. 23 nearly vanishes. This

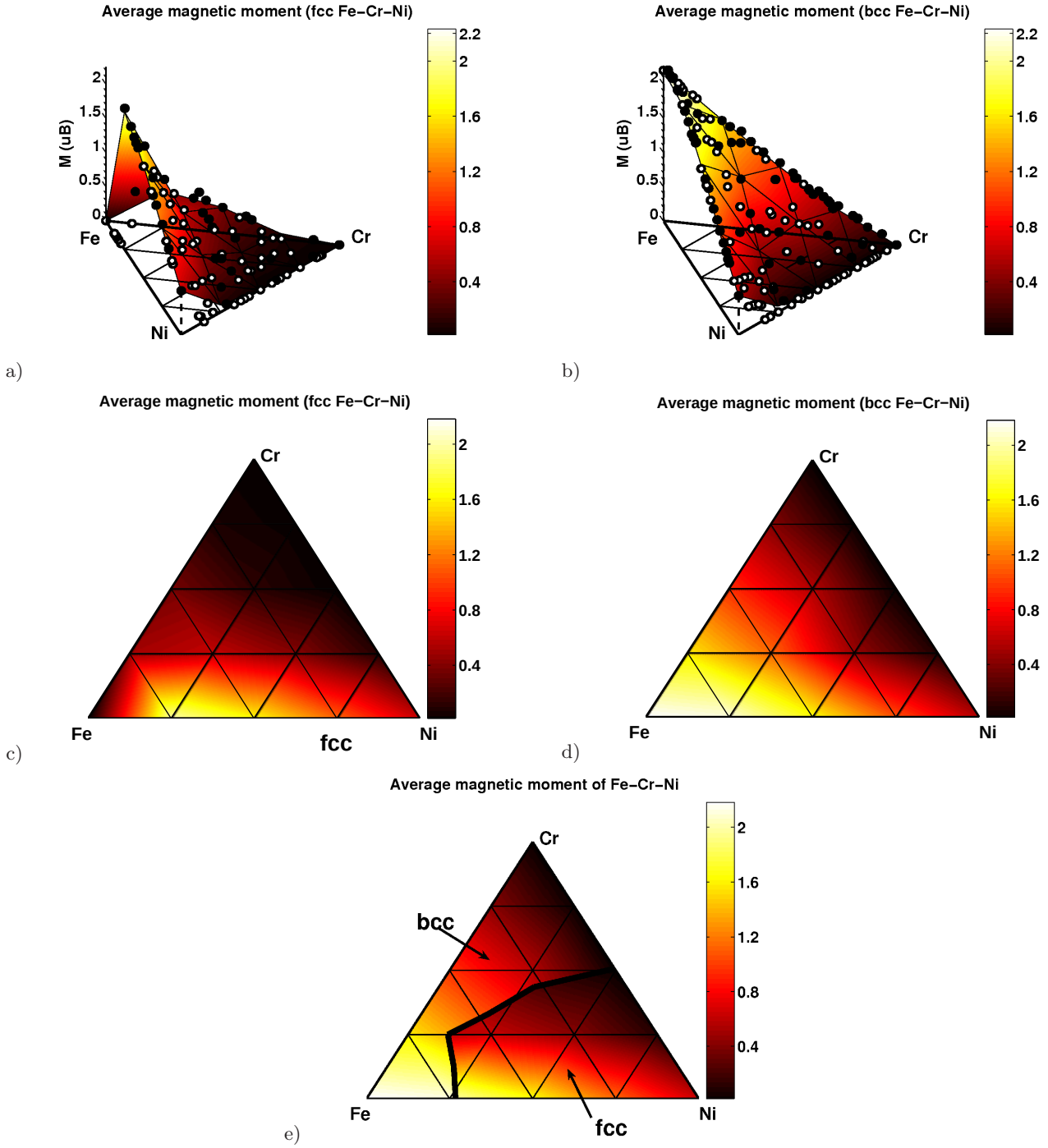

FIG. 9. (Color online) Magnetic moment per atom in the most stable fcc (a, c) and bcc (b, d) ordered alloy structures predicted by DFT calculations at 0K for each alloy composition. Filled and open circles in (a, b) correspond to DFT data above and below the interpolated values represented by the respective surfaces. (c, d) are the orthogonal projections of (a, b). (e) The average atomic magnetic moment of fcc and bcc structures is discontinuous across the fcc-bcc phase transition line, shown in the figure as solid black line.

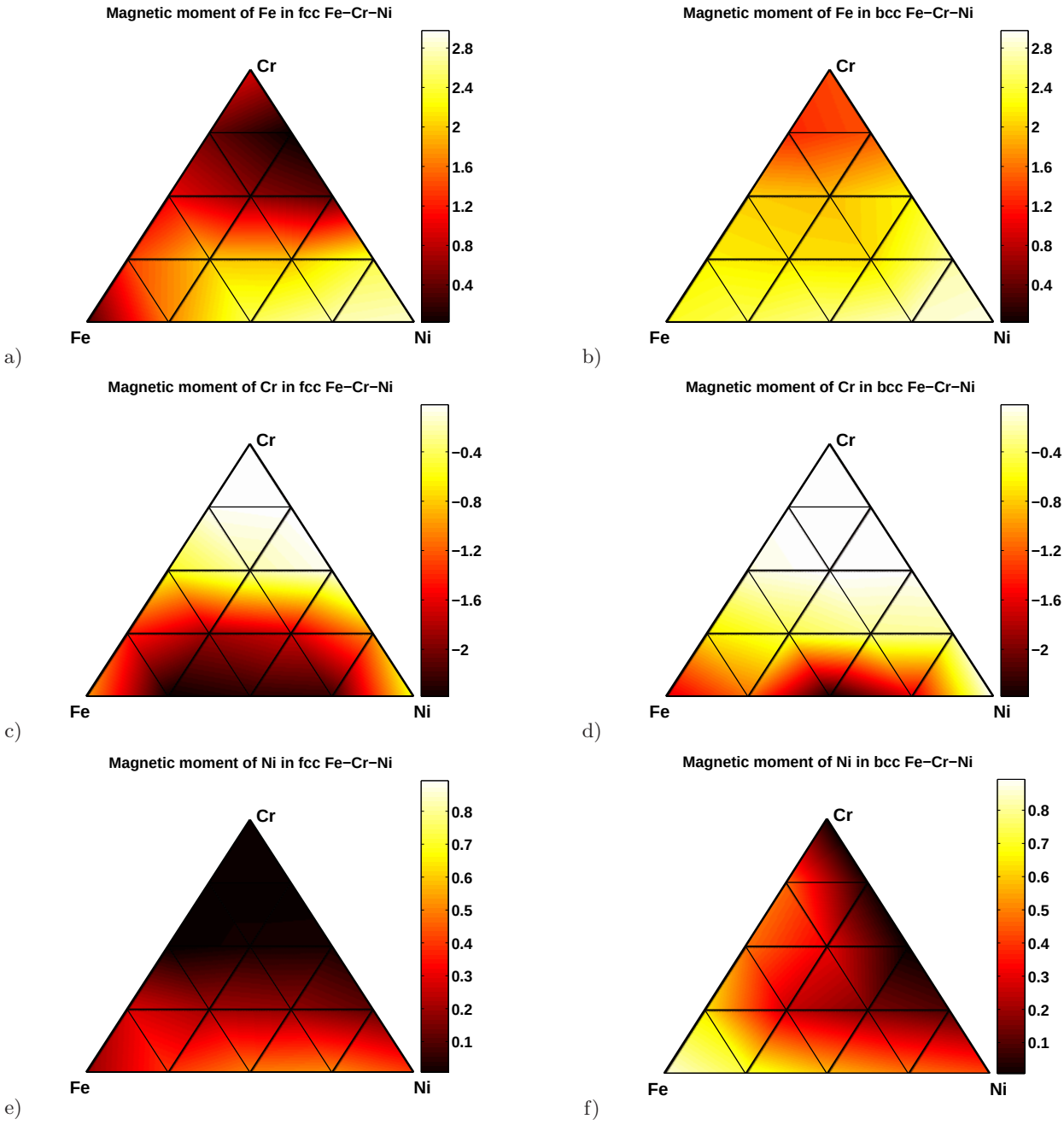

FIG. 10. (Color online) Magnetic moments of Fe (a, b), Cr (c, d) and Ni (e, f) on fcc (a, c, e) and bcc (b, d, f) lattices.

also explains the experimentally observed decrease of atomic ordering in $FeNi_3$ alloys following the addition of Cr[25]. Large 1NN effective pairwise Fe-Cr and Cr-Ni interactions (V_1^{Fe-Cr} and V_1^{Cr-Ni} are correspondingly smaller and larger in ternary alloys in comparison with binary alloys) and the relatively large 2NN effective interaction between these atoms explains also the pronounced atomic ordering in the majority of fcc Fe-Cr-Ni alloys.

The sign pattern of the first three nearest-neighbour chemical pairwise interactions in all the binary and ternary fcc alloys remains the same. The first and third nearest-neighbour (3NN) pair interactions are positive and the second nearest neighbour interaction is negative. This favours the unlike atoms occupying the 1NN and 3NN coordination shells, and the like atoms occupying the 2NN shell, see the Eq.19. Such pattern of signs of NN interactions favours not only intermetallic $L1_2$ and $MoPt_2$-like phases, which occur in fcc binary alloys, but also the $L1_2$-based (Cu_2ZnNi-like) Fe_2CrNi ternary phase, which is the global ground state of ternary Fe-Cr-Ni alloys.

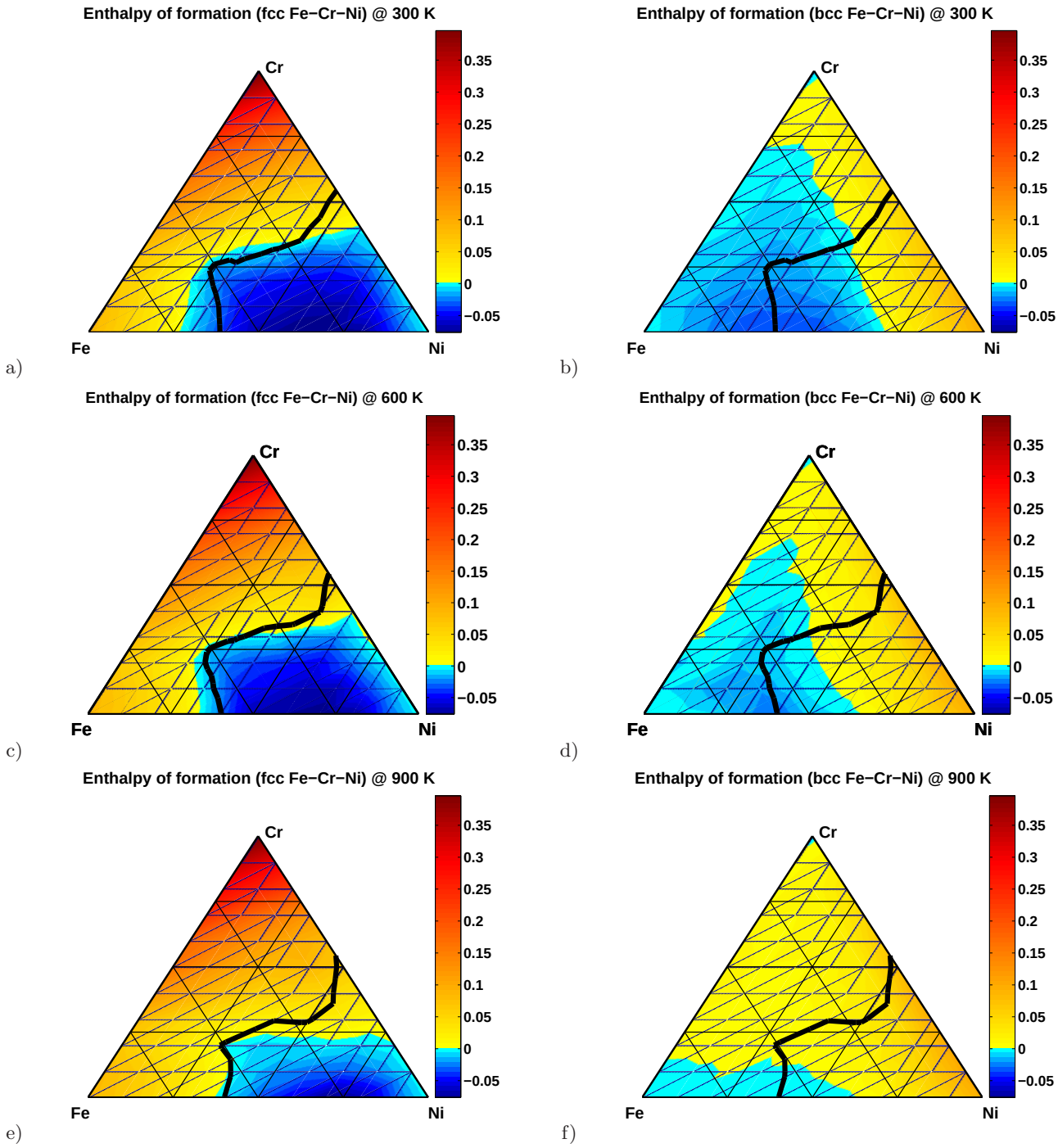

FIG. 11. (Color online) Enthalpies of formation of fcc (a, c, e) and bcc (b, c, f) alloys calculated using MC simulations at 300K (a, b), 600K (c, d) and 900K (e, f). Black solid line corresponds to the phase transition line between Ni-rich fcc alloys and the region of stability of bcc alloys.

V. FINITE TEMPERATURE MAGNETIC PROPERTIES OF FE-CR-NI ALLOYS

Using the DFT database developed above and Magnetic Cluster Expansion (MCE), we now investigate how magnetic properties depend on temperature, and how magnetism affects the phase stability of Fe-Cr-Ni ternary alloys. MCE has been successfully applied to a number of binary systems, including bcc and fcc Fe-Cr[72] and fcc Fe-Ni[64]. In MCE[96,97], each alloy configuration is defined by both chemical (σ_i) and magnetic ($\mathbf{M}_i$) degrees of freedom. MCE parameters were derived from DFT data on 30 ordered ternary Fe-Cr-Ni structures (see Supplementary Material Part

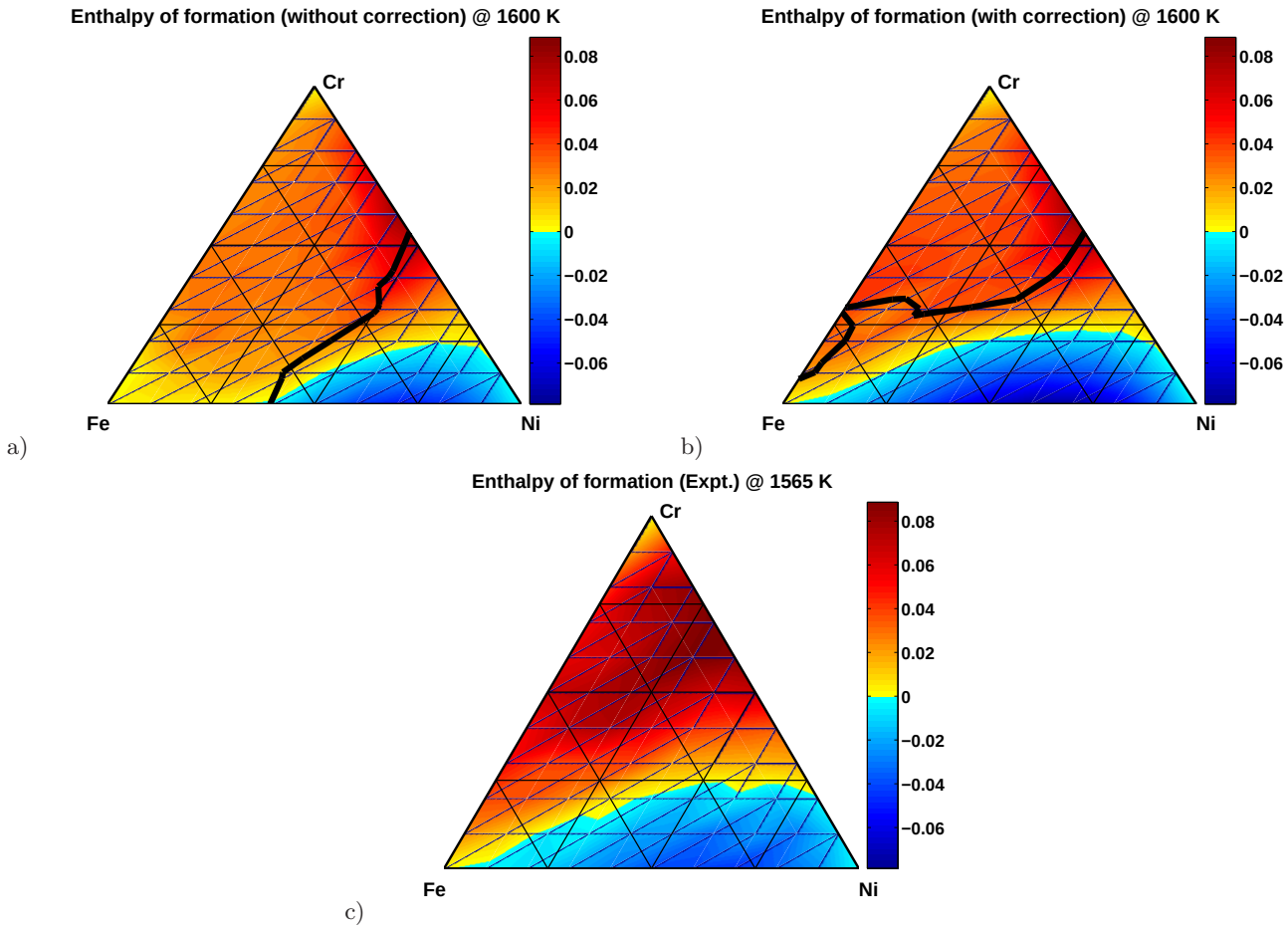

FIG. 12. (Color online) Enthalpies of formation (in eV/atom) for the most stable crystal structures of Fe-Cr-Ni alloys computed using MC simulations at 1600K without (a) and with (b) the magnetic correction, compared to experimental data (c) from Refs. 85 and 86. Black solid line shows the phase transition line separating Ni-rich fcc alloys and the region of stability of bcc alloys.

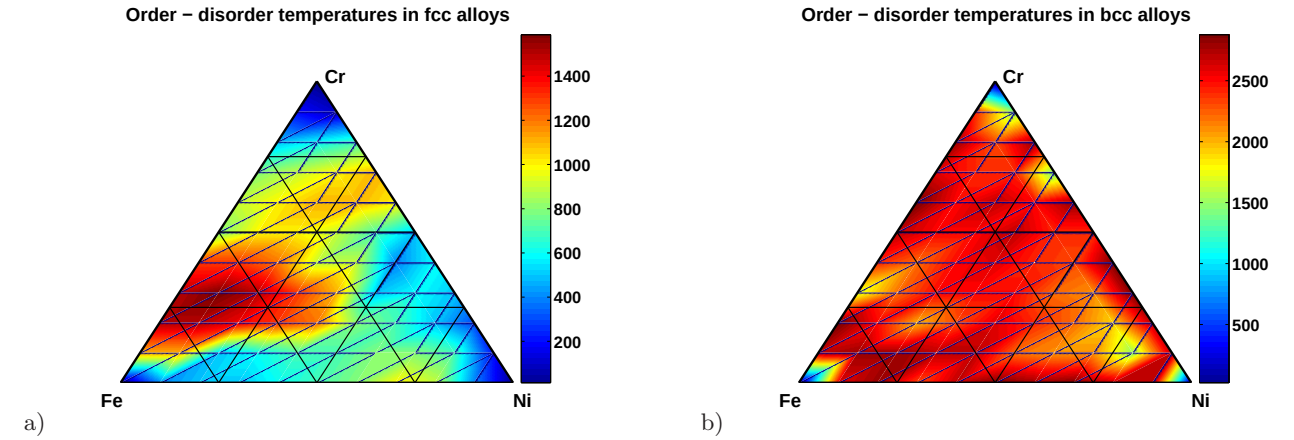

FIG. 13. (Color online) Order-disorder temperatures of fcc (a) and bcc (b) Fe-Cr-Ni alloys computed using Monte Carlo simulations. Order-disorder temperatures for pure elements are assumed to be 0 K.

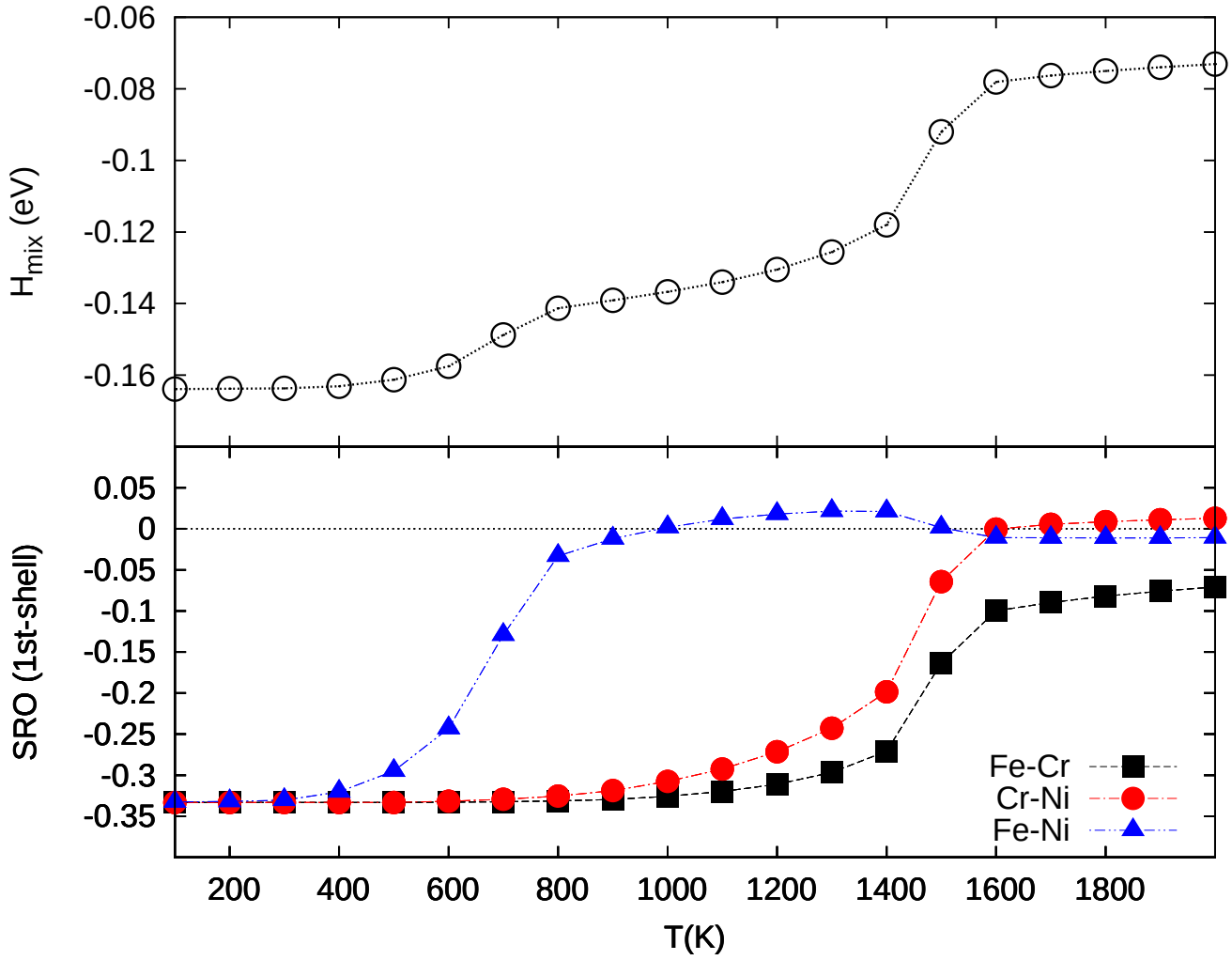

FIG. 14. (Color online) Enthalpies of mixing and short-range order parameters (SRO) computed as functions of temperature for Fe-Cr, Cr-Ni and Fe-Ni atomic pairs in the first coordination shell of fcc $Fe_{50}Cr_{25}Ni_{25}$ alloy.

1), spanning the entire concentration range, together with the data on pure elements. Parametrization was also based on 29 binary fcc Fe-Ni configurations used in a recent application of MCE to fcc Fe-Ni[64]. To simplify applications of MCE to ternary alloys and to reduce the number of fitting parameters, we use an MCE Hamiltonian that includes only pairwise interactions. In this approximation, the energy of an arbitrary alloy configuration $(\{\sigma_i\},\{\mathbf{M}_i\})$ can be written in the Heisenberg-Landau form as follows

$$\begin{aligned} H_{MCE}\left(\{\sigma_i\},\{\mathbf{M}_i\}\right) = & \sum_i \mathcal{I}^{(1)}_{\sigma_i} + \sum_{ij\in 1NN} \mathcal{I}^{(1NN)}_{\sigma_i\sigma_j} + \sum_{ij\in 2NN} \mathcal{I}^{(2NN)}_{\sigma_i\sigma_j} + \ldots \\ & + \sum_i A_{\sigma_i}\mathbf{M}_i^2 + \sum_i B_{\sigma_i}\mathbf{M}_i^4 + \ldots \\ & + \sum_{ij\in 1NN} \mathcal{J}^{(1NN)}_{\sigma_i\sigma_j}\mathbf{M}_i\cdot\mathbf{M}_j + \sum_{ij\in 2NN} \mathcal{J}^{(2NN)}_{\sigma_i\sigma_j}\mathbf{M}_i\cdot\mathbf{M}_j + \ldots, \end{aligned} \tag{24}$$

where σ_i, σ_j = Fe, Cr and Ni, and the non-magnetic and Heisenberg magnetic interaction parameters $\mathcal{I}_{ij}$ and $\mathcal{J}_{ij}$ for each coordination shell are represented by 3×3 matrices. We take into account interactions that extend up to the fourth nearest neighbour coordination shell. In all, there are 24 independent non-magnetic and 24 independent magnetic interaction parameters. At the first stage of fitting, the on-site magnetic terms A, B, C,... were fitted using, as input, the curves of energy versus magnetic moment in the ferromagnetic states of pure Fe, Ni, and Cr.

TABLE VI. Short-range order parameters for selected binary alloys calculated using Monte Carlo simulations at various temperatures T, compared with experimental data.

	T (K)	MC (this study)	MC (Others)	Expt.	MC	MC[35]	Expt.
fcc alloys			α_1			α_2	
$Fe_{25}Ni_{75}$	1300	-0.096		-0.099[c]	0.097		0.116[c]
$Fe_{30}Ni_{70}$		-0.102		-0.088[c]	0.105		0.049[c]
$Fe_{50}Ni_{50}$		-0.071		-0.073[c]	0.082		0.042[c]
$Fe_{60}Ni_{40}$		-0.043		-0.058[c]	0.058		0.089[c]
$Fe_{65}Ni_{35}$		-0.018		-0.051[c]	0.049		0.034[c]
$Fe_{70}Ni_{30}$		-0.002		-0.033[c]	0.031		0.005[c]
$Fe_{65}Ni_{35}$	1100	-0.022		-0.058[d]	0.076		0.052[d]
$Cr_{33}Ni_{67}$	1100	-0.036	-0.115[a]	-0.08[e]	0.042	0.12[35]	0.05[e]
$Cr_{25}Ni_{75}$	1000	-0.047	-0.105[a]	-0.07[f]	0.051	0.10[35]	0.045[f]
$Cr_{20}Ni_{80}$	800	-0.029	-0.125[a]	-0.10[g]	0.057	0.115[35]	0.085[g]
bcc alloys			α_{1+2}				
$Fe_{95}Cr_5$	700	-0.044	-0.049[b]	-0.05[h]			
$Fe_{93.75}Cr_{6.25}$		-0.056					
$Fe_{90}Cr_{10}$		-0.071	-0.080[b]	0.00[h]			
$Fe_{85}Cr_{15}$		0.138	0.309[b]	0.065[h]			

[a] Ref. 35 MC simulations.
[b] Ref. 32 MC simulations.
[c] Refs. 91 and 92 annealed at 1273 K.
[d] Ref. 93 annealed at 1026 K.
[e] Ref. 94 annealed at 1073 K.
[f] Ref. 94 annealed at 993 K.
[g] Ref. 95 annealed at 828 K.
[h] Ref. 77 annealed at 703 K.

For chromium, only quadratic and quartic terms were used, while for iron and nickel the Landau expansion was extended up to the 8^{th}-order in magnetic moment[64]. Dependence of on-site terms on the atomic environment was neglected in order to reduce the number of parameters in the Hamiltonian. Following the established procedure[64], interaction terms $\mathcal{I}$ and $\mathcal{J}$ were fitted using the DFT data on total energies and magnetic moments on each site in the simulation cell. Most of the alloy structures used for parametrizing the Fe-Cr-Ni MCE Hamiltonian (Eq. 24) belonged to the Fe-rich corner of the ternary alloy composition triangle. Hence we expect that MCE predictions are going to be most reliable for alloys where Fe content exceeds 50 at.%. Monte Carlo MCE simulations were performed using a 16384 atom simulation cell (16×16×16 fcc unit cells). As an example of application of MCE to modelling low-temperature magnetic properties of a ternary alloy, we investigated how the total magnetic moment of disordered $(Fe_{0.5}Ni_{0.5})_{1-x}Cr_x$ alloy varies as a function of Cr content. We noted in III.E that the average magnetic moment of the alloy decreases rapidly with increasing chromium concentration. In MCE Monte Carlo simulations, ordered FeNi alloy with $L1_0$ structure was chosen as the initial alloy configuration. Magnetic moment per atom in this structure was found to be 1.61 μ_B, close to the DFT value of 1.63 μ_B. Chromium content was then varied by replacing equal numbers of Fe and Ni atoms in their sublattices with Cr atoms, with positions of chromium atoms chosen at random. Figure 17 shows the predicted variation of magnetic moment in the resulting alloy at low temperatures. With increasing Cr content, magnetization rapidly decreases, resulting in a completely non-magnetic system at x_{Cr}=0.4, in agreement with *ab initio* results of Section III.E, also illustrated in Figure 17.

While random alloy with composition $Fe_{50}Cr_{25}Ni_{25}$ is almost completely anti-ferromagnetic, ordered alloy of the same composition has non-vanishing total magnetic moment. At low temperature, magnetic moments are collinear, with Cr moments being antiferromagnetically ordered with respect to Fe moments and having almost the same magnitude, while magnetic moments of Ni atoms are much smaller and ferromagnetically ordered with respect to the Fe moments. Finite temperature magnetic properties are investigated using Monte Carlo simulations performed using large simulation cells. Magnetic moments of each of the three components of ordered Fe_2CrNi alloy, treated as functions of temperature, are shown in Figure 18. Their values at low temperature are in reasonable agreement with DFT, for example magnetic moments of Fe, Cr and Ni obtained from MCE simulations are 2.7, -2.2 and 0.37

TABLE VII. Short-range order parameters for Fe-Cr, Fe-Ni and Cr-Ni pairs in ternary alloys calculated using Monte Carlo simulations, and compared with experimental observations. (Fe,Cr)-Ni means average SRO involving Ni and average (Fe,Cr) atoms as defined by Eq. 23.

		α_1		α_2	
		MC	Expt.	MC	Expt.
$Fe_{56}Cr_{21}Ni_{23}$					
Fe-Ni	1300	0.003	0.017[a]	-0.094	-0.002[a]
Fe-Cr		-0.280	-0.009[a]	0.781	0.043[a]
Cr-Ni		-0.134	-0.113[a]	0.600	0.148[a]
$Fe_{42.5}Cr_{7.5}Ni_{50}$					
Fe-Ni		-0.069		0.073	
Fe-Cr	1300	-0.080		0.087	
Cr-Ni		0.015		0.085	
(Fe,Cr)-Ni		-0.057	-0.049[b]	0.075	0.015[b]
Fe-Ni		-0.099		0.144	
Fe-Cr	900	-0.158		0.281	
Cr-Ni		0.039		0.134	
(Fe,Cr)-Ni		-0.077	-0.093[c]	0.142	0.134[c]
Fe-Ni		-0.213		0.681	
Fe-Cr	600	-0.403		0.975	
Cr-Ni		0.180		0.680	
(Fe,Cr)-Ni		-0.150	-0.121[d]	0.681	0.148[d]
$Fe_{38}Cr_{14}Ni_{48}$					
Fe-Ni		-0.054		0.054	
Fe-Cr	1300	-0.076		0.141	
Cr-Ni		-0.014		0.115	
(Fe,Cr)-Ni		-0.043[b]	-0.048	0.070	0.018[b]
Fe-Ni		-0.076		0.116	
Fe-Cr	900	-0.276		0.701	
Cr-Ni		-0.023		0.382	
(Fe,Cr)-Ni		-0.062	-0.091[c]	0.188	0.082[c]
Fe-Ni		-0.149		0.648	
Fe-Cr	600	-0.489		0.983	
Cr-Ni		0.097		0.814	
(Fe,Cr)-Ni		-0.082	-0.126[d]	0.693	0.089[d]
$Fe_{34}Cr_{20}Ni_{46}$					
Fe-Ni		-0.035		0.033	
Fe-Cr	1300	-0.060		0.168	
Cr-Ni		-0.031		0.136	
(Fe,Cr)-Ni		-0.033	-0.042[b]	0.071	0.017[b]
Fe-Ni		-0.035		0.024	
Fe-Cr	900	-0.300		0.838	
Cr-Ni		-0.146		0.563	
(Fe,Cr)-Ni		-0.077	-0.088[c]	0.224	0.086[c]
Fe-Ni		-0.138		0.538	
Fe-Cr	600	-0.401		0.994	
Cr-Ni		-0.133		0.799	
(Fe,Cr)-Ni		-0.137	-0.152[d]	0.634	0.098[d]

[a] Ref.23 annealed at 1273 K.
[b] Ref.24 quenched from 1323 K.
[c] Ref.24 annealed at 873 K.
[d] Ref.24 irradiated at 583 K with 2.5 MeV electrons.

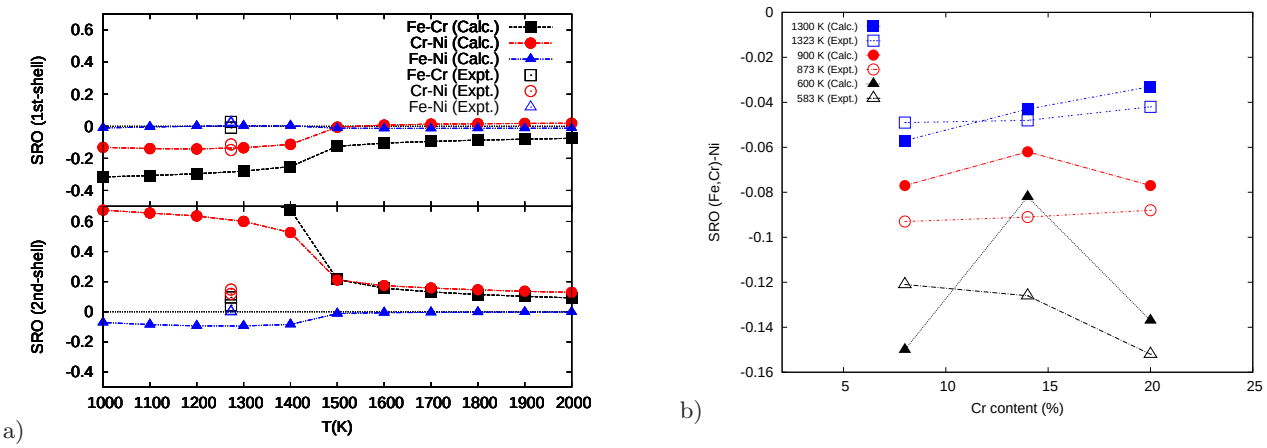

FIG. 15. (Color online) (a) Short-range order parameters as functions of temperature calculated for Fe-Cr, Cr-Ni and Fe-Ni pairs occupying two coordination shells in $Fe_{0.56}Cr_{0.21}Ni_{0.23}$ alloy, compared with experimental values from Ref. 23; (b) 1NN SRO between Ni and average (Fe,Cr) atoms in $Fe_{42.5}Cr_{7.5}Ni_{50}$, $Fe_{38}Cr_{14}Ni_{48}$ and $Fe_{34}Cr_{20}Ni_{46}$ calculated at 600K, 900K and 1300K, and compared with experimental data taken from Ref. 24 and presented as a function of Cr content; (Fe,Cr)-Ni indicates average SRO between Ni and average (Fe,Cr) atoms obtained from Eq. 23.

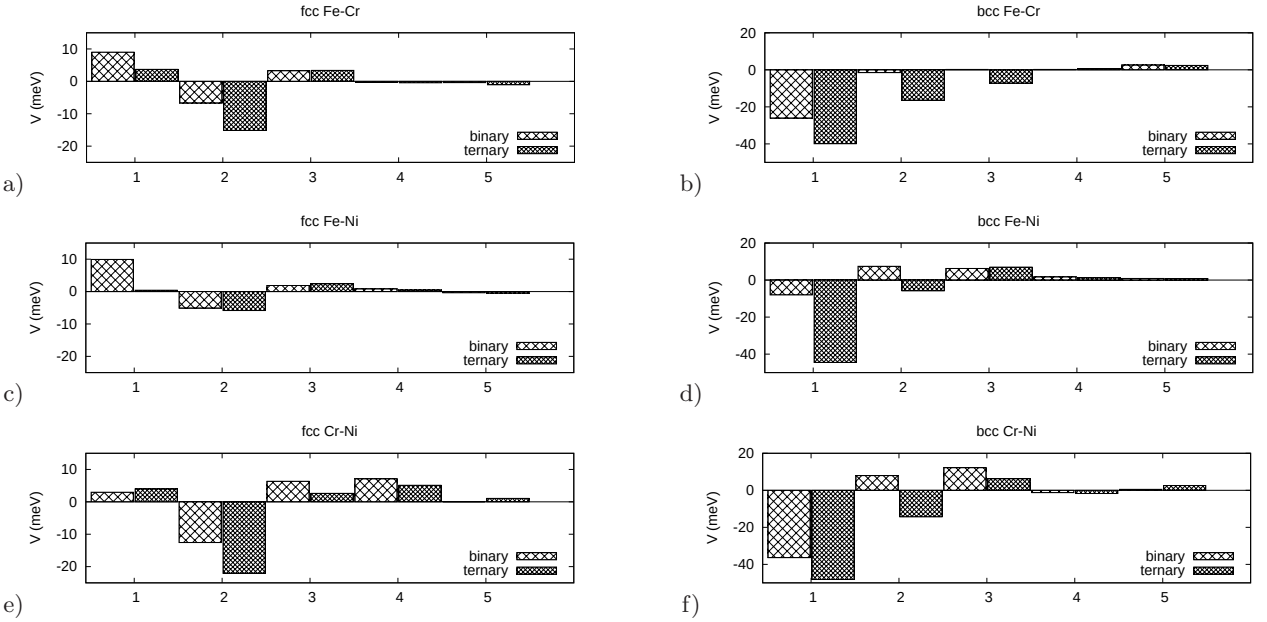

FIG. 16. Effective interactions between different pairs of atoms: Fe-Cr (a,b), Fe-Ni (c,d) and Cr-Ni (e,f) on fcc (a,c,e) and bcc (b,d,f) lattices in ternary Fe-Cr-Ni and binary alloys.

μ_B, whereas DFT predictions are 2.08, -2.44 and 0.15 μ_B, respectively. Table III provides further details. The alloy remains magnetic up to very high temperatures close to 1000 K. The effect is similar to that found in fcc Fe-Ni, where chemically ordered $FeNi_3$ alloy has higher Curie temperature than pure Ni. In the ternary Fe_2CrNi alloy, the highly stable ferromagnetic structure owes its stability to strong anti-ferromagnetic interactions between (Fe, Ni) and Cr atoms.

In summary, in this section we described applications of Magnetic Cluster Expansion to ternary alloys. Although the parametrization of MCE Hamiltonian involved a number of approximations, MCE predictions are in good agreement with the low temperature DFT data. In the high temperature limit, Monte Carlo simulations show that interplay between chemical and magnetic degrees of freedom gives rise to high Curie temperature of ordered Fe_2CrNi alloy. Further improvement in the accuracy of MCE model is expected to provide means for investigating temperature-dependent magnetic and configurational order over the entire range of alloy compositions.

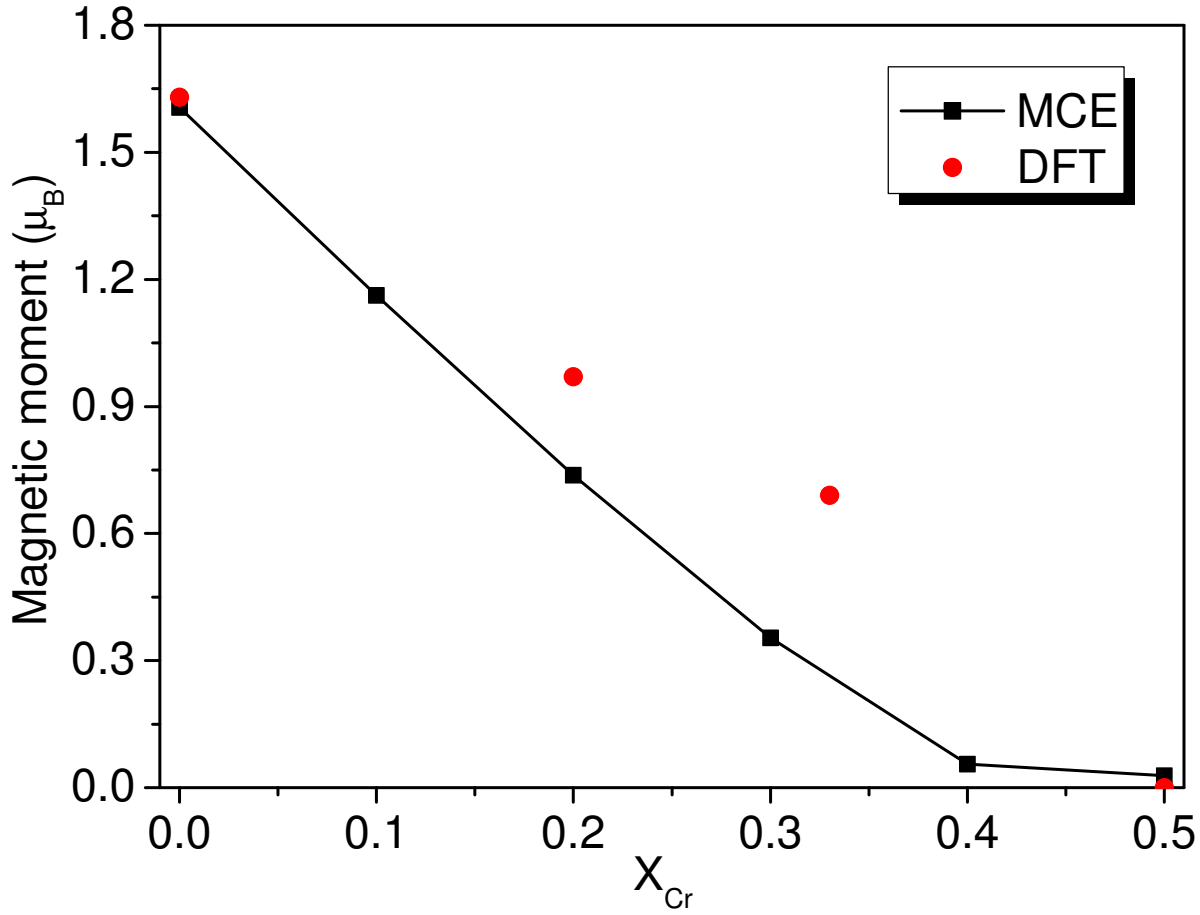

FIG. 17. (Color online) Total magnetic moment per atom in $(Fe_{0.5}Ni_{0.5})_{1-x}Cr_x$ alloy as a function of chromium content x, predicted by MCE. DFT results (Sec. III.E) are shown by red circles.

VI. CONCLUSIONS

We have systematically investigated fcc and bcc phase stability of ternary magnetic Fe-Cr-Ni alloys, using a combination of first-principles DFT calculations and Monte Carlo simulations, involving both conventional and magnetic cluster expansions. Detailed derivation of a general expression for the CE enthalpy of mixing is given for a ternary alloy system, where average cluster functions are defined as products of orthogonal point functions. An explicit analytical relationship between chemical SRO and effective pair-wise interactions, involving different species, is established and applied to the exploration of SRO properties of Fe-Cr-Ni alloys and interpretation of experimental data. Using a DFT database of 248 fcc and 246 bcc structures, we explored fcc and bcc phase stability of this ternary alloy system. Effective cluster interactions parameters for fcc and bcc binaries and ternaries have been derived and cross-validated against DFT data. Strong deviations from Vegard's law for atomic volumes treated as functions of alloy composition stem from magnetic interactions. The predicted average total and local magnetic moments treated as functions of Ni concentration in the ground-state bcc and fcc structures of Fe-Ni alloys are in good agreement with experimental data. Calculations not only identify ground-state structures of the three binary alloys, but also predict new fcc-like Fe_2CrNi compound as the most stable ground-state ternary intermetallic system with negative enthalpy of formation of -0.164 eV/atom and the lowest ordering temperature of 650K. Both DFT and MCE simulations show that the phase stability of Fe_2CrNi structure is primarily determined by strong anti-ferromagnetic interactions between Fe and Ni atoms with Cr atoms.

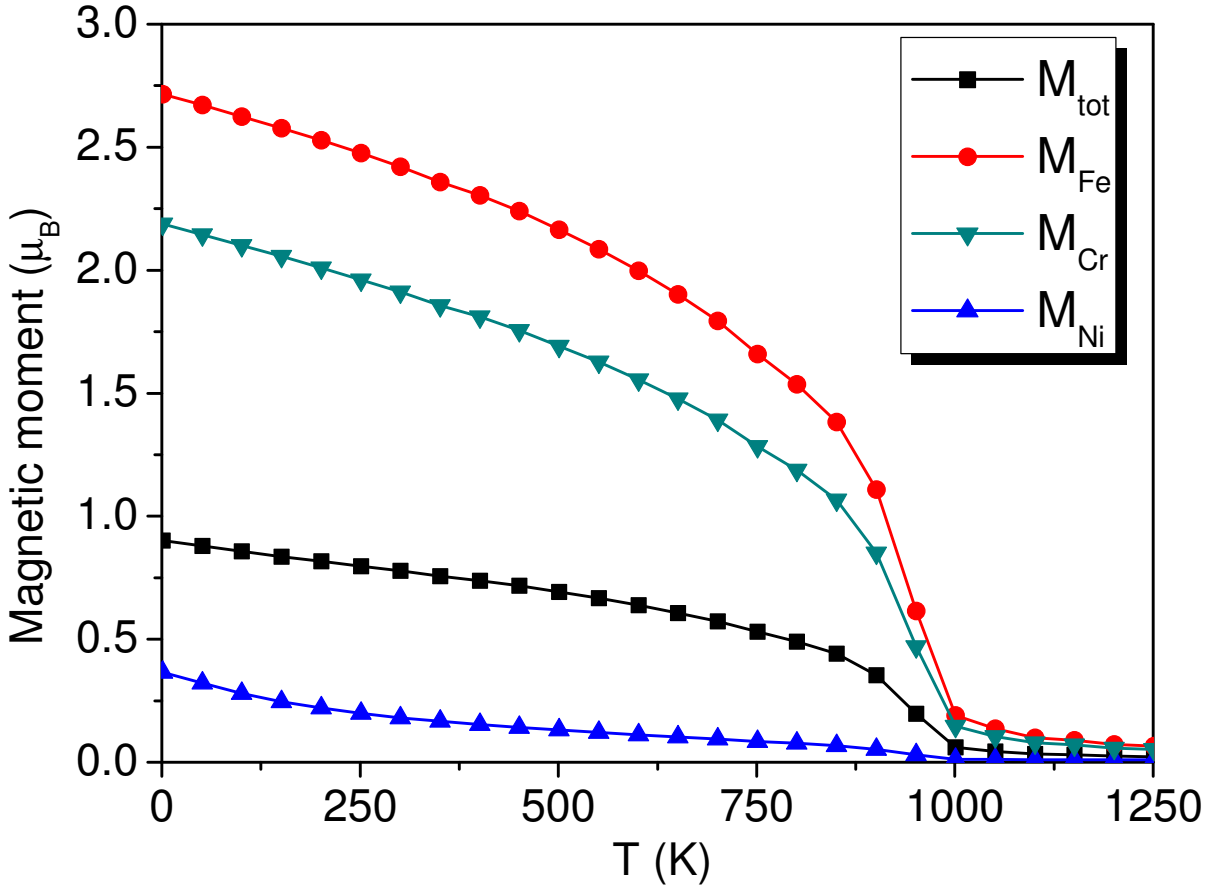

FIG. 18. (Color online) Temperature dependence of the total magnetic moment of ordered Fe_2CrNi alloy, and magnetic moments of atoms forming the alloy.

Enthalpies of formation were evaluated to identify the relative phase stability of ternary fcc and bcc phases at various temperatures. Excellent agreement between calculations and experimental data on enthalpies of formation at 1600K shows that magnetic contribution to the excess free energy plays an important part in correcting the deficiencies of conventional CE treatment of Fe-Cr-Ni alloys. We have calculated the Warren-Cowley short range order parameters at different ordering temperatures and found good agreement with experimental data on binary and ternary alloys. Particular attention has been devoted to $Fe_{56}Cr_{21}Ni_{23}$, $Fe_{38}Cr_{14}Ni_{48}$ and $Fe_{34}Cr_{20}Ni_{46}$ alloys corresponding to the centre of the composition triangle, to rationalize how SRO varies in Fe-Cr, Fe-Ni and Ni-Cr binary alloys at various temperatures. The fact that the SRO parameter decreases significantly for Fe-Ni pairs as a function of Cr concentration agrees with experimental observations. This important aspect of alloy thermodynamics is also related to the fact that interaction between Cr and both Fe and Ni is strongly anti-ferromagnetic, explaining large negative values of SRO predicted for Fe-Cr and Ni-Cr atomic pairs.

The above study provides a starting point for the treatment of thermodynamics of Fe-Cr-Ni, involving chemical and magnetic interactions in this traditionally important but very complex ternary alloy system. By comparing MC configurations generated using effective cluster interactions with those created by the SQS method, we are able to demonstrate that the former are energetically more stable for all the magnetic structures considered here, as illustrated by the case of $Fe_{70}Cr_{20}Ni_{10}$ alloy. This provides information needed for choosing structures for modelling point defects in ternary alloys, where defect structures are sensitive not only to the average alloy composition but also to the local chemical and magnetic environment of a defect site[31,98,99].

ACKNOWLEDGMENTS

This work was funded by the Accelerated Metallurgy Project, which is co-funded by the European Commission in the 7th Framework Programme (Contract NMP4-LA-2011-263206), by the European Space Agency and by the individual partner organisations. This work was also part-funded by the RCUK Energy Programme (Grant Number EP/I501045) and by the European Unions Horizon 2020 research and innovation programme under grant agreement number 633053. To obtain further information on the data and models underlying this paper please contact PublicationsManager@ccfe.ac.uk. The views and opinions expressed herein do not necessarily reflect those of the European Commission. The authors would like to thank Charlotte Becquart, Maria Ganchenkova and George Smith for stimulating and helpful discussions. DNM would like to acknowledge Juelich supercomputer centre for the provision of High-Performances Computer for Fusion (HPC-FF) facilities as well as the International Fusion Energy Research Centre (IFERC) for the provision of a supercomputer (Helios) at Computational Simulation Centre (CSC) in Rokkasho (Japan).

---

* jan.wrobel@ccfe.ac.uk, jan.wrobel@inmat.pw.edu.pl

[1] C. E. Guillaume, C. R. Hebd. Seances Acad. Sci. **125**, 235 (1897).
[2] H. Arnold and G. W. Elmen, J. Franklin Inst. **195**, 621 (1923).
[3] R. L. Klueh and D. R. Harries, *High-Chromium Ferritic and Martensitic Steels for Nuclear Applications* (American Society for Testing of Materials (ASTM), USA, 2001).
[4] T. Toyama, Y. Nozawa, W. van Renterghem, Y. Matsukawa, M. Hatakeyama, Y. Nagai, A. Al Mazouzi, and S. van Dyck, J. Nucl. Mater. **425**, 71 (2012).
[5] A. F. Rowcliffe, L. K. Mansur, D. T. Hoelzer, and R. K. Nanstad, J. Nucl. Mater. **392**, 341 (2009).
[6] D. Stork, P. Agostini, J.-L. Boutard, D. Buckthorpe, E. Diegele, S. L. Dudarev, C. English, G. Federici, M. R. Gilbert, S. Gonzalez, A. Ibarra, C. Linsmeier, A. L. Puma, G. Marbach, L. W. Packer, B. Raj, M. Rieth, M. Q. Tran, D. J. Ward, and S. J. Zinkle, Fusion Engineering and Design (2014), 10.1016/j.fusengdes.2013.11.007.
[7] Y. Satoh, S. Abe, H. Matsui, and I. Yamagata, J. Nucl. Mater. **367-370**, 972 (2007).
[8] M. Ferry, *Direct Strip Casting of Metals and Alloys* (Woodhead Publishing Limited, Cambridge, 2006).
[9] W. P. Rees, B. D. Burns, and A. J. Cook, J. Iron Steel Inst. **162**, 325 (1949).
[10] B. Hattersley and W. Hume-Rothery, J. Iron Steel Inst. **204**, 683 (1966).
[11] A. J. Cook and B. R. Brown, J. Iron Steel Inst. **171**, 345 (1952).
[12] F. Körmann, A. A. H. Breidi, S. L. Dudarev, N. Dupin, G. Ghosh, T. Hickel, P. Korzhavyi, J. A. Muñoz, and I. Ohnuma, Phys. Stat. Sol. B **251**, 53 (2014).
[13] G. Cacciamani, A. Dinsdale, M. Palumbo, and A. Pasturel, Intermetallics **18**, 1148 (2010).
[14] P. Franke and H. J. Seifert, Calphad **35**, 148 (2011).
[15] T. P. C. Klaver, D. J. Hepburn, and G. J. Ackland, Phys. Rev. B **85**, 174111 (2012).
[16] D. J. Hepburn, D. Ferguson, S. Gardner, and G. J. Ackland, Phys. Rev. B **88**, 024115 (2013).
[17] L. Vitos, P. Korzhavyi, and B. Johansson, Phys. Rev. Lett. **88**, 155501 (2002).
[18] L. Vitos, P. Korzhavyi, and B. Johansson, Phys. Rev. Lett. **96**, 117210 (2006).
[19] L. Delczeg, B. Johansson, and L. Vitos, Phys. Rev. B **85**, 174101 (2012).
[20] J. B. Piochaud, T. P. C. Klaver, G. Adjanor, P. Olsson, C. Domain, and C. S. Becquart, Phys. Rev. B **89**, 024101 (2014).
[21] A. Zunger, S. H. Wei, L. G. Ferreira, and J. E. Bernard, Phys. Rev. Lett. **65**, 353 (1990).
[22] O. Dimitrov and C. Dimitrov, J. Phys. F: Met. Phys. **16**, 969 (1986).
[23] P. Cenedese, F. Bley, and S. Lefebvre, Acta Cryst. **A40**, 228 (1984).
[24] A. Z. Menshikov, C. Dimitrov, and A. E. Teplykh, J. Phys. III France **7**, 1899 (1997).
[25] A. D. Marwick, R. C. Piller, and T. E. Cranshaw, J. Phys. F: Met. Phys. **17**, 37 (1987).
[26] J. M. Sanchez, F. Ducastelle, and D. Gratias, Physica **128A**, 334 (1984).
[27] J. W. D. Connolly and A. R. Williams, Phys. Rev. B **27**, 5169 (1983).
[28] A. V. Ruban and I. A. Abrikosov, Rep. Prog. Phys. **71**, 046501 (2008).
[29] T. P. C. Klaver, R. Drautz, and M. W. Finnis, Phys. Rev. B **74**, 094435 (2006).
[30] D. Nguyen-Manh, M. Y. Lavrentiev, and S. L. Dudarev, J. Comput.-Aided Mater. Des. **14**, 159 (2007).
[31] D. Nguyen-Manh, M. Y. Lavrentiev, M. Muzyk, and S. L. Dudarev, Journal of Materials Science **47**, 7385 (2012).
[32] M. Y. Lavrentiev, R. Drautz, D. Nguyen-Manh, T. P. C. Klaver, and S. L. Dudarev, Phys. Rev. B **75**, 014208 (2007).
[33] S. V. Barabash, R. V. Chepulskii, V. Blum, and A. Zunger, Phys. Rev. B **80**, 220201 (2009).
[34] M. Ekholm, H. Zapolsky, A. V. Ruban, I. Vernyhora, D. Ledue, and I. A. Abrikosov, Phys. Rev. Let. **105**, 167208 (2010).
[35] M. Rahaman, B. Johansson, and A. V. Ruban, Phys. Rev. B **89**, 064103 (2014).
[36] A. K. Majumdar and P. v. Blanckenhagen, Phys. Rev. B **29**, 4079 (1984).
[37] A. van de Walle, Calphad **33**, 266 (2009).
[38] N. Sandberg, M. Slabanja, and R. Holmestad, Comp. Mater. Sci. **40**, 309 (2007).
[39] C. Wolverton and D. de Fontaine, Phys. Rev. B **49**, 8627 (1994).

[40] F. Ducastelle, *Order and phase stability in alloys* (North-Holland, Amsterdam, 1991).
[41] M. Asta, C. Wolverton, D. de Fontaine, and H. Dreyssé, Phys. Rev. B **44**, 4907 (1991).
[42] D. de Fontaine, J. Appl. Cryst. **4**, 15 (1971).
[43] A. van de Walle, M. Asta, and G. Ceder, Calphad **26**, 539 (2002).
[44] G. Kresse and J. Furthmüller, Comp. Mater. Sci. **6**, 15 (1996).
[45] G. Kresse and J. Furthmüller, Phys. Rev. B **54**, 11169 (1996).
[46] J. P. Perdew, K. Burke, and M. Ernzerhof, Phys. Rev. Lett. **77**, 3865 (1996).
[47] H. J. Monkhorst and J. D. Pack, Phys. Rev. B **13**, 5188 (1976).
[48] S. V. Barabash, V. Blum, S. Müller, and A. Zunger, Phys. Rev. B **74**, 035108 (2006).
[49] G. Ceder, G. D. Garbulsky, D. Avis, and K. Fukuda, Phys. Rev. B **49**, 1 (1994).
[50] H. C. Herper, E. Hoffmann, and P. Entel, Phys. Rev. B **60**, 3839 (1999).
[51] V. L. Moruzzi, P. M. Marcus, and J. Kübler, Phys. Rev. B **39**, 6957 (1989).
[52] M. Acet, H. Zähres, E. F. Wassermann, and W. Pepperhoff, Phys. Rev. B **49**, 6012 (1994).
[53] J. Crangle and G. C. Hallam, Proc. Roy. Soc. A **272**, 119 (1963).
[54] S. C. Abrahams, L. Guttman, and J. S. Kasper, Phys. Rev. **127**, 2052 (1962).
[55] C. Kittel, *Introduction to Solid State Physics* (Wiley, New York, 1971).
[56] H. P. J. Wijn, ed., *Magnetic Properties of Metals*, Landolt-Börstein. Numerical Data and Functional Relationships in Science and Technology. Volume 19 (Springer Berlin Heidelberg, Berlin, Heidelberg, 1991).
[57] A. Chamberod, J. Laugier, and J. M. Penisson, J. Magn. Magn. Mater. **10**, 139 (1979).
[58] T. Mohri and Y. Chen, Journal of Alloys and Compounds **383**, 23 (2004).
[59] J. D. Tucker, *Ab initio - based modelling of radiation effects in the Ni-Fe-Cr system* (University of Wisconsin-Madison, Wisconsin, 2008).
[60] I. A. Abrikosov, A. E. Kissavos, F. Liot, B. Alling, S. I. Simak, O. Peil, and A. V. Ruban, Phys. Rev. B **76**, 014434 (2007).
[61] V. Crisan, P. Entel, H. Ebert, H. Akai, D. D. Johnson, and J. B. Staunton, Phys. Rev. B **66**, 014416 (2002).
[62] A. V. Ruban, M. Katsnelson, W. Olovsson, S. I. Simak, and I. A. Abrikosov, Phys. Rev. B **71**, 054402 (2005).
[63] A. V. Ruban, S. Khmelevskyi, P. Mohn, and B. Johansson, Phys. Rev. B **76**, 014420 (2007).
[64] M. Y. Lavrentiev, J. S. Wróbel, D. Nguyen-Manh, and S. L. Dudarev, Phys. Chem. Chem. Phys. **16**, 16049 (2014).
[65] T. B. Massalski, H. Okamoto, P. K. Subramanion, and L. Kacprzak, eds., *Binary Alloy Phase Diagrams*, 2nd ed. (American Society for Metals, Metals Park, OH, 1990).
[66] K. B. Reuter and D. B. Williams, Metall. Trans. A **20**, 719 (1989).
[67] T. Mohri and Y. Chen, Calphad **33**, 244 (2009).
[68] Z. W. Lu, S. H. Wei, A. Zunger, S. Frota-Pessoa, and L. G. Ferreira, Phys. Rev. B **44**, 512 (1991).
[69] P. Entel, E. Hoffmann, P. Mohn, K. Schwarz, and V. L. Moruzzi, Phys. Rev. B **47**, 8706 (1993).
[70] D. Nguyen-Manh, M. Y. Lavrentiev, and S. L. Dudarev, C. R. Physique **9**, 379 (2008).
[71] D. Nguyen-Manh and S. L. Dudarev, Phys. Rev. B **80**, 104440 (2009).
[72] M. Y. Lavrentiev, D. Nguyen-Manh, and S. L. Dudarev, Phys. Rev. B **81**, 184202 (2010).
[73] P. Olsson, I. A. Abrikosov, L. Vitos, and J. Wallenius, J. Nucl. Mater. **321**, 84 (2003).
[74] P. Olsson, I. A. Abrikosov, and J. Wallenius, Phys. Rev. B **73**, 104416 (2006).
[75] H. Zhang, B. Johansson, and L. Vitos, Phys. Rev. B **79**, 224201 (2009).
[76] P. Erhart, B. Sadigh, and A. Caro, Appl. Phys. Lett. **92**, 141904 (2008).
[77] I. Mirebeau, M. Kennion, and G. Parette, Phys. Rev. Lett. **53**, 687 (1984).
[78] W. B. Pearson, *A Handbook of Lattice Spacings and Structures of Metals and Alloys* (Pergamon Press, London, 1958).
[79] A. T. Aldred, Phys. Rev. B **14**, 219 (1976).
[80] A. T. Aldred, B. D. Rainford, J. S. Kouvel, and T. J. Hicks, Phys. Rev. B **14**, 228 (1976).
[81] F. Kajzar and G. Parette, Phys. Rev. B **22**, 5471 (1980).
[82] V. Rode, A. Deryabin, and G. Damashke, IEEE Trans. Magn. **12**, 404 (1976).
[83] C. Bansal and G. Chandra, Solid State Comm. **19**, 107 (1976).
[84] Q. Chen and B. Sundman, J. Phase Equil. **22**, 631 (2001).
[85] O. Kubaschewski and L. E. H. Stuart, J. Chem. Eng. Data **12**, 418 (1967).
[86] W. A. Dench, Trans. Faraday Soc. **59**, 1279 (1963).
[87] J. Tomiska, J. Alloys Compd. **379**, 176 (2004).
[88] B. D. Sharma, K. Sonnenberg, G. Antesberger, and W. Kesternich, Phil. Mag. A **37**, 777 (1978).
[89] A. van de Walle and G. Ceder, Rev. Mod. Phys. **74**, 11 (2002).
[90] G. Bonny, R. C. Pasianot, L. Malerba, A. Caro, P. Olsson, and M. Y. Lavrentiev, J. Nucl. Mater. **385**, 268 (2009).
[91] V. I. Gomankov, I. M. Puzei, and V. N. Sigaev, Pisma Zh. Eksp. Teor. Fiz. **13**, 600 (1971).
[92] A. Z. Menshikov, V. Y. Arkhipov, A. I. Zakharov, and S. K. Sidorov, Fiz. Met. Metalloved. **34**, 309 (1972).
[93] J. L. Robertson, G. E. Ice, C. J. Sparks, X. Jiang, P. Zschack, F. Bley, S. Lefebvre, and M. Bessiere, Phys. Rev. Lett. **82**, 2911 (1999).
[94] R. Caudron, M. Sarfati, M. Barrachin, A. Finel, F. Ducastelle, and F. Solal, J. Phys. I France **2**, 1145 (1992).
[95] B. Schönfeld, L. Reinhard, G. Kostorz, and W. Buhrer, Phys. Stat. Sol. B **148**, 457 (1988).
[96] M. Y. Lavrentiev and S. L. Dudarev, J. Nucl. Mater. **386-388**, 22 (2009).
[97] M. Y. Lavrentiev, D. Nguyen-Manh, and S. L. Dudarev, Solid State Phenom. **172-174**, 1002 (2011).
[98] M. Muzyk, D. Nguyen-Manh, K. J. Kurzydłowski, N. L. Baluc, and S. L. Dudarev, Phys. Rev. B **84**, 104115 (2011).
[99] M. Muzyk, D. Nguyen-Manh, J. Wróbel, K. J. Kurzydłowski, N. L. Baluc, and S. L. Dudarev, J. Nucl. Mater. **442**, S680

(2013).

Appendix A: Averaged cluster functions for triple clusters

Similarly to Eq. 10, the average cluster functions for triple clusters (n-th nearest neighbours) are defined as

$$\begin{aligned}\left\langle \Gamma_{3,n}^{(ijk)} \right\rangle &= \langle \gamma_i, \gamma_j, \gamma_k \rangle \\ &= \sum_p \sum_q \sum_r y_n^{pqr} \gamma_i(\sigma_p)\gamma_j(\sigma_q)\gamma_k(\sigma_r),\end{aligned} \tag{A1}$$

where y_n^{pqr} is the probability of finding three p, q and r atoms in the n-th nearest neighbour coordination shell. Specifically,

$$\begin{aligned}\left\langle \Gamma_{3,n}^{(111)} \right\rangle &= \frac{1}{8}\left(-8y_n^{AAA} + 12y_n^{AAB} + 12y_n^{AAC} - 6y_n^{ABB}\right. \\ &- 6y_n^{ABC} - 6y_n^{ACC} + y_n^{BBB} \\ &+ \left. 3y_n^{BBC} + 3y_n^{BCC} + y_n^{CCC}\right) \\ \left\langle \Gamma_{3,n}^{(112)} \right\rangle &= \frac{\sqrt{3}}{8}\left(-4y_n^{AAB} + 4y_n^{AAC} + 4y_n^{ABB} - 4y_n^{ACC}\right. \\ &- \left. y_n^{BBB} - y_n^{BBC} + y_n^{BCC} + y_n^{CCC}\right) \\ \left\langle \Gamma_{3,n}^{(122)} \right\rangle &= \frac{3}{8}\left(-2y_n^{ABB} + 2y_n^{ABC} - 2y_n^{ACC} + y_n^{BBB}\right. \\ &- \left. y_n^{BBC} - y_n^{BCC} + y_n^{CCC}\right) \\ \left\langle \Gamma_{3,n}^{(222)} \right\rangle &= \frac{3\sqrt{3}}{8}\left(-y_n^{BBB} + 3y_n^{BBC}\right. \\ &- \left. 3y_n^{BCC} + y_n^{CCC}\right)\end{aligned} \tag{A2}$$

Rewriting Eq. 6 using average point, pair and triple correlation functions from Eqs. 9, 12 and A2, respectively, the configurational enthalpy of mixing of ternary alloys can now be written as a function of concentrations, c_i, and the average pair and 3-body probabilities, y_n^{ij} and y_n^{ijk}, respectively, as

$$\begin{aligned}\Delta H_{CE}(\vec{\sigma}) &= J_1^{(0)} + J_1^{(1)}\left(1 - 3c_A\right) + J_1^{(2)}\frac{\sqrt{3}}{2}\left(c_C - c_B\right) \\ &+ \sum_n^{pairs}\left[\frac{1}{4}m_{2,n}^{(11)}J_{2,n}^{(11)}\left(1 + 3y_n^{AA} - 6y_n^{AB} - 6y_n^{AC}\right)\right. \\ &+ \left.\frac{\sqrt{3}}{4}m_{2,n}^{(12)}J_{2,n}^{(12)}\left(-y_n^{BB} + y_n^{CC} + 2y_n^{AB} - 2y_n^{AC}\right) + \frac{3}{4}m_{2,n}^{(22)}J_{2,n}^{(22)}\left(y_n^{BB} + y_n^{CC} - 2y_n^{BC}\right)\right] \\ &+ \sum_n^{triples}\left[\frac{1}{8}m_{3,n}^{(111)}J_{3,n}^{(111)}\left(-8y_n^{AAA} + 12y_n^{AAB} + 12y_n^{AAC}\right.\right. \\ &- \left. 6y_n^{ABB} - 6y_n^{ABC} - 6y_n^{ACC} + y_n^{BBB} + 3y_n^{BBC} + 3y_n^{BCC} + y_n^{CCC}\right) \\ &+ \frac{\sqrt{3}}{8}\left(m_{3,n}^{(112)}J_{3,n}^{(112)} + m_{3,n}^{(121)}J_{3,n}^{(121)} + m_{3,n}^{(211)}J_{3,n}^{(211)}\right) \\ &\cdot \left(-4y_n^{AAB} + 4y_n^{AAC} + 4y_n^{ABB} - 4y_n^{ACC} - y_n^{BBB} - y_n^{BBC} + y_n^{BCC} + y_n^{CCC}\right) \\ &+ \frac{3}{8}\left(m_{3,n}^{(122)}J_{3,n}^{(122)} + m_{3,n}^{(212)}J_{3,n}^{(212)} + m_{3,n}^{(221)}J_{3,n}^{(221)}\right) \\ &\cdot \left(-2y_n^{ABB} + 2y_n^{ABC} - 2y_n^{ACC} + y_n^{BBB} - y_n^{BBC} - y_n^{BCC} + y_n^{CCC}\right) \\ &+ \left.\frac{3\sqrt{3}}{8}m_{3,n}^{(222)}J_{3,n}^{(222)}\left(-y_n^{BBB} + 3y_n^{BBC} - 3y_n^{BCC} + y_n^{CCC}\right)\right] \\ &+ \sum_n^{multibody}\cdots\end{aligned} \tag{A3}$$

Appendix B: Input ternary structures for bcc alloys

Input ternary CE structures for bcc alloys were constructed from binary structures[30], by replacing atoms A or B at non-equivalent atomic positions by atoms C.

a) A_3B_{13} - based on 13sc222
Space group: $P4/mmm$ (no. 123)
Wyckoff positions:
A_1 $1c$ $(\frac{1}{2}, \frac{1}{2}, 0)$
A_2 $1d$ $(\frac{1}{2}, \frac{1}{2}, \frac{1}{2})$
A_3 $1a$ (0,0,0)
B_1 $2f$ $(0, \frac{1}{2}, 0)$
B_2 $8r$ $(\frac{3}{4}, \frac{3}{4}, \frac{3}{4})$
B_3 $2e$ $(0, \frac{1}{2}, \frac{1}{2})$
B_4 $1b$ $(0, 0, \frac{1}{2})$

b) A_5B_{11} - based on 11sc222
Space group: $P4/mmm$ (no. 123)
Wyckoff positions:
A_1 $1a$ (0,0,0)
A_2 $2f$ $(0, \frac{1}{2}, 0)$
A_3 $2e$ $(0, \frac{1}{2}, \frac{1}{2})$
B_1 $8r$ $(\frac{3}{4}, \frac{3}{4}, \frac{3}{4})$
B_2 $1b$ $(0, 0, \frac{1}{2})$
B_3 $1c$ $(\frac{1}{2}, \frac{1}{2}, 0)$
B_4 $1d$ $(\frac{1}{2}, \frac{1}{2}, \frac{1}{2})$

c) A_3B_5 - based on PdTi
Space group: $P4/mmm$ (no. 123)
Wyckoff positions:
A_1 $2h$ $(\frac{1}{2}, \frac{1}{2}, \frac{1}{8})$
A_2 $1b$ $(0, 0, \frac{1}{2})$
B_1 $1a$ $(0, 0, 0)$
B_2 $2g$ $(0, 0, \frac{1}{4})$
B_3 $2h$ $(\frac{1}{2}, \frac{1}{2}, \frac{3}{8})$

d) A_3B_5 - based on tP8-L53-1
Space group: $P4/mmm$ (no. 123)
Wyckoff positions:
A_1 $2h$ $(\frac{1}{2}, \frac{1}{2}, \frac{7}{8})$
A_2 $1a$ $(0, 0, 0)$
B_1 $2g$ $(0, 0, \frac{1}{4})$
B_2 $2h$ $(\frac{1}{2}, \frac{1}{2}, \frac{3}{8})$
B_3 $1b$ $(0, 0, \frac{1}{2})$

e) A_3B_4 - based on tP14-L34-2
Space group: $I4/mmm$ (no. 139)
Wyckoff positions:
A_1 $4e$ $(0, 0, 0)$
A_2 $2b$ $(0, 0, \frac{1}{2})$
B_1 $4e$ $(0, 0, \frac{3}{4})$
B_2 $4e$ $(0, 0, \frac{1}{4})$

f) A_7B_9 - based on 9sc222
Space group: $Pm-3m$ (no. 221)
Wyckoff positions:
A_1 $1a$ $(0, 0, 0)$
A_2 $3d$ $(\frac{1}{2}, 0, 0)$
A_3 $3c$ $(0, \frac{1}{2}, \frac{1}{2})$
B_1 $8g$ $(\frac{1}{4}, \frac{1}{4}, \frac{1}{4})$
B_2 $1b$ $(\frac{1}{2}, \frac{1}{2}, \frac{1}{2})$

g) A_4B_4 - based on tP8-L44-1

Space group: $P4/nmm$ (no. 129)
Wyckoff positions:
A_1 $2c$ ($\frac{1}{4}$, $\frac{1}{4}$, $\frac{1}{4}$)
A_2 $2c$ ($\frac{1}{4}$, $\frac{1}{4}$, $\frac{1}{2}$)
B_1 $2c$ ($\frac{1}{4}$, $\frac{1}{4}$, $\frac{3}{4}$)
B_2 $2c$ ($\frac{1}{4}$, $\frac{1}{4}$, 0)
h) A_5B_4 - based on VZn
Space group: $I4/mmm$ (no. 139)
Wyckoff positions:
A_1 $2a$ (0,0,0)
A_2 $8h$ ($\frac{1}{3}$, $\frac{1}{3}$, 0)
B_1 $8i$ ($\frac{2}{3}$, 0, 0)
f) A_4B_3 - based on tI14-L34-1
Space group: $I4/mmm$ (no. 139)
Wyckoff positions:
A_1 $4e$ (0,0,$\frac{3}{4}$)
A_2 $4e$ (0,0,0)
B_1 $4e$ (0,0,$\frac{1}{4}$)
B_2 $2b$ (0,0,$\frac{1}{2}$)
g) A_4B_3 - based on tI14-L34-2
Space group: $I4/mmm$ (no. 139)
Wyckoff positions:
A_1 $4e$ (0,0,$\frac{3}{4}$)
A_2 $4e$ (0,0,$\frac{1}{4}$)
B_1 $4e$ (0,0,0)
B_2 $2b$ (0,0,$\frac{1}{2}$)
h) A_3B_2 - based on tI10-L32-1
Space group: $I4/mmm$ (no. 139)
Wyckoff positions:
A_1 $4e$ (0,0,-$\frac{1}{10}$)
A_2 $2b$ (0,0,$\frac{1}{2}$)
A_2 $4e$ (0,0,$\frac{7}{10}$)
i) A_3B_2 - based on tP8-L53-1
Space group: $P4/mmm$ (no. 123)
Wyckoff positions:
A_1 $2g$ (0,0,$\frac{1}{4}$)
A_2 $2h$ ($\frac{1}{2}$, $\frac{1}{2}$, $\frac{3}{8}$)
A_3 $1b$ (0,0,$\frac{1}{2}$)
B_2 $2h$ ($\frac{1}{2}$, $\frac{1}{2}$, $\frac{7}{8}$)
B_3 $1a$ (0,0,0)

Appendix C: Effective cluster interactions for binary alloys

Table VIII contains a complete set of effective cluster interactions for fcc and bcc Fe-Ni, Fe-Cr, and Cr-Ni binary alloys.

TABLE VIII. Number of points, $|\omega|$, labels n, multiplicities, $m_{|\omega|,n}$, and effective cluster interactions, $J_{|\omega|,n}$ (in meV), for fcc and bcc binary alloys: Fe-Cr, Fe-Ni and Cr-Ni.

$\|\omega\|$	n	$m_{\|\omega\|,n}$		$J_{\|\omega\|,n}$					
		fcc	*bcc*	*fcc* Fe-Cr	*bcc* Fe-Cr	*fcc* Fe-Ni	*bcc* Fe-Ni	*fcc* Cr-Ni	*bcc* Cr-Ni
1	0	1	1	-64.130	85.814	-61.528	-49.833	-121.455	67.238
1	1	1	1	-40.636	50.986	-52.464	-45.967	8.527	-84.613
2	1	6	4	9.034	-26.088	9.926	-8.198	2.982	-36.395
2	2	3	3	-6.667	-1.530	-5.087	7.622	-12.547	7.956
2	3	12	6	3.308	0.219	1.901	6.252	6.350	12.229
2	4	6	12	-0.332	0.219	0.851	1.724	7.129	-1.245
2	5	12	4	-0.386	2.601	-0.347	0.731	0.048	0.510
3	1	8	12	-4.548	0.721	3.310	2.927	4.165	5.918
3	2	12	12	3.547	-1.976	0.572	1.870	3.926	1.599
3	3	24		0.681		0.853		-2.319	
4	1	2	6	0.557	1.278	-2.667	1.026	3.770	-0.191
4	2	12		0.181		-0.007		0.945	
5	1	6	12	1.693	-2.907	-0.982	-0.622	-5.171	-0.542